Final Technical Report submitted to the Department of Energy –

Office of Basic Energy Sciences; Dr. Lane C. Wilson, Program Manager

Period of performance for Sept 15, 2010 – Sept 14, 2013

DOE award # DE-SC0001988 to Brown University

# "Optoacoustic Microscopy for Investigation of Material Nanostructures – Embracing the Ultrasmall, Ultrafast, and the Invisible"

by

Professors Humphrey Maris and Arto Nurmikko, Brown University

Department of Physics and the School of Engineering, Providence, RI 02912

Humphrey_Maris@brown.edu ; Arto_Nurmikko@brown.edu

**I. Summary of Accomplishments:**

The goal of this grant was the development of a new type of scanning acoustic microscope for nanometer resolution ultrasound imaging, based on ultrafast optoacoustics (>GHz). In the microscope, subpicosecond laser pulses was used to generate and detect very high frequency ultrasound with nanometer wavelengths. We report here on the outcome of the 3-year DOE/BES grant which involved the design, multifaceted construction, and proof-of-concept demonstration of an instrument that can be used for quantitative imaging of nanoscale material features – including features that may be buried so as to be inaccessible to conventional lightwave or electron microscopies. The research program has produced a prototype scanning optoacoustic microscope which, in combination with advanced computational modeling, is a system-level new technology (two patents issues) which offer novel means for precision metrology of material nanostructures, particularly those that are of contemporary interest to the frontline micro- and optoelectronics device industry. For accomplishing the ambitious technical goals, the research roadmap was designed and implemented in two phases. In Phase I, we constructed a "non-focusing" optoacoustic microscope instrument ("POAM"), with nanometer vertical (z-) resolution, while limited to approximately 10 micrometer scale lateral recolution. The Phase I version of the instrument which was guided by extensive acoustic and optical numerical modeling of the basic underlying acoustic and optical physics, featured nanometer scale close loop positioning between the optoacoustic transducer element and a nanostructured material sample under investigation. In phase II, we implemented and demonstrated a scanning version of the instrument ("SOAM") where incident acoustic energy is focused, and scanned on lateral (x-y) spatial scale in the 100 nm range as per the goals of the project. In so doing we developed advanced numerical simulations to provide computational models of the focusing of multi-GHz acoustic waves to the nanometer scale and innovated a series fabrication approaches for a new type of broadband high-frequency acoustic focusing microscope objective by applying methods on nanoimprinting and focused-ion beam techniques.

In the following, the Phase I and Phase II instrument development is reported as Section II. The first segment of this section describes the POAM instrument and its development, while including much of the underlying ultrafast acoustic physics which is common to all of our work for this grant. Then, the science and engineering of the SOAM instrument is described, including the methods of fabricating new types of acoustic microlenses. The results section is followed by reports on publications (Section III), Participants (Section IV), and statement of full use of the allocated grant funds (Section V).

**II.A. Phase I: High Precision Planar Optoacoustic Microscope (POAM)**

During the course of the grant research, we have shown that, by adopting a Fabry-Perot optical cavity, the measurement of the acoustic wave reflection from the sample immersed in water can

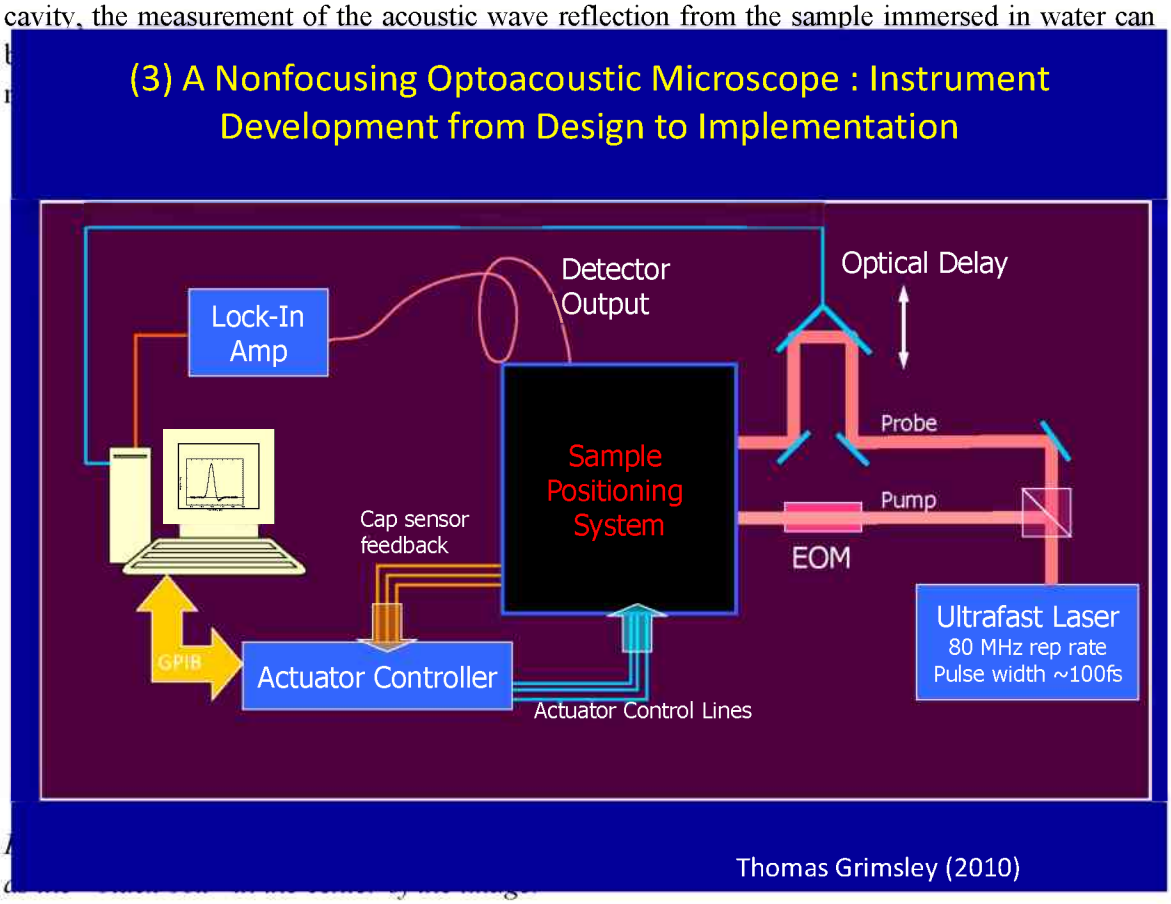


optical system in *Figure 1*. This feature was incorporated to complete the construction of the planar precision instrument which has exceptional closed-loop control of the distance between the optoacoustic broadband (>GHz) transceiver element and the sample under investigation. As shown belwo, this engineering feat enabled vertical resolution $\Delta z \sim 5$ nanometer while necessitating the capability to maintain parallelism between the transceiver and the sample plane within 0.1 mrad). The (non-focusing microscope) Phase I version of the instrument described next was limited in its lateral resolution to conventional diffraction limited optical focusing of the pump-and probe beams, that is it lacked ability to precision scan in the xy-plane of sub-micrometer features. However, with the nanometer scale z-resolution we were able to achieve set of new milestones for optoacoustic microscopy for semiconductor nanostructures as shown here

The planar optoacoustic microscope system design is shown in *Figure 2*. The signal enhancing optical/acoustic Fabry-Perot cavity is mounted to an annular plate (cavity plate) which rests on three posts that are bolted to a circular base (base plate). The cavity plate is coupled to the posts with a using a type II Kelvin clamp. Tungsten carbide balls are epoxied to the cavity plate in recessed spherical grooves. The balls will seat in tungsten carbide v-blocks that are attached to the invar posts, which are in turn bolted to the base plate. The kinematic components have been

chosen such that the repeatability of the cavity platform when it is removed and reseated should be on the order of the surface roughness of the V-blocks, if not better.

Three piezoelectric actuators are bolted to a base (actuator base) which is bolted to the base plate. The three actuators form the legs of a tripod that supports the sample which rests on a plate (sample plate). The separation between the cavity plate and the sample plate is measured by three capacitive sensors. The output of the sensors is fed into a digital controller which actively moves the actuators to maintain the separation between the cavity and the sample plates.

The sample plate is coupled to the actuators using another Kelvin clamp, where truncated balls made of stainless steel are bolted to the tops of the actuators. These balls reside in small stainless

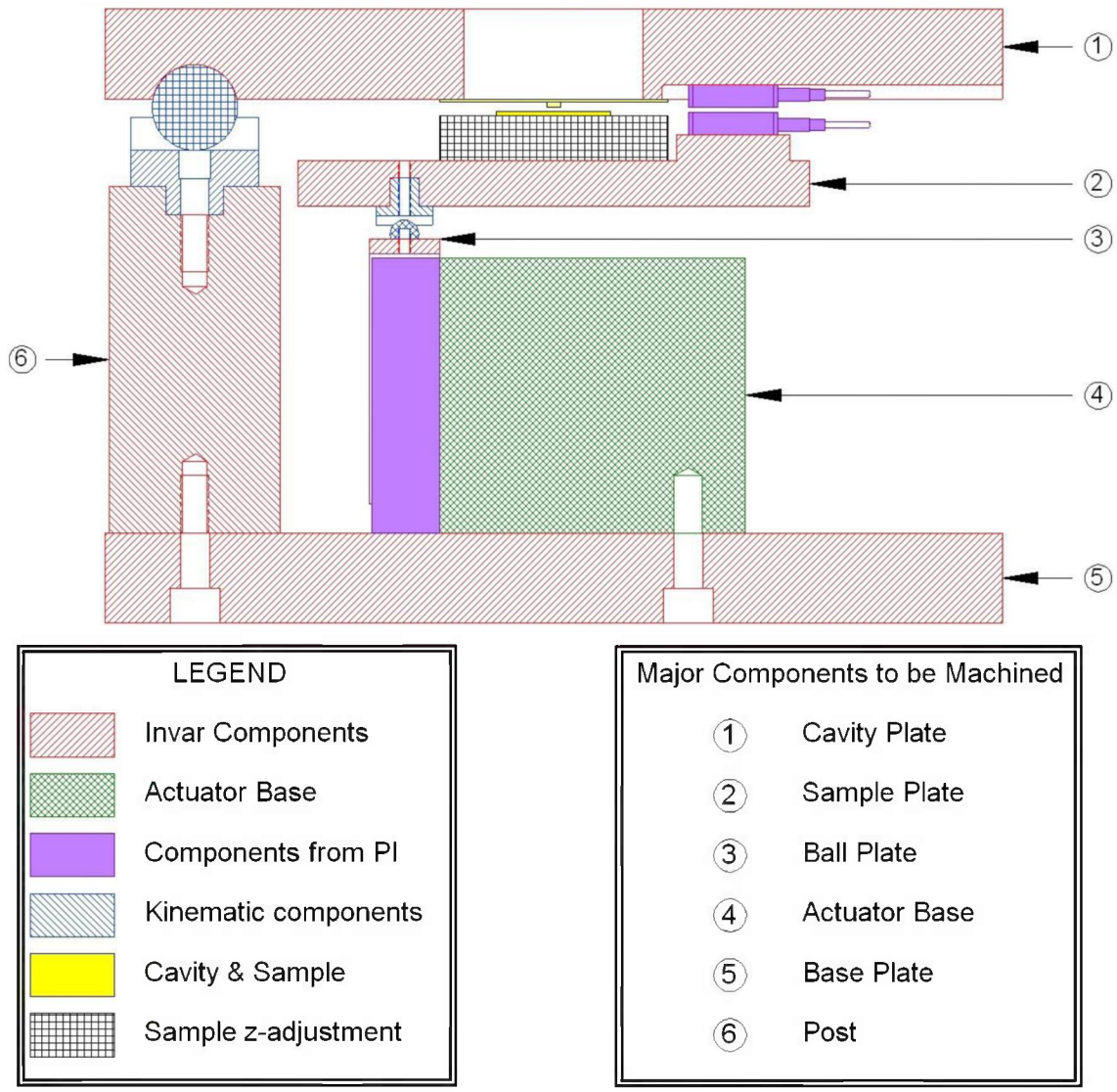


*Figure 2 – Cross sectional view of the sample positioning system. The upper and lower plates are 20 cm in diameter, the posts are 1.5" in diameter, and the whole assembly stands about 11 cm tall.*

stainless steel V-blocks that are bolted to the sample plate. A kinematic coupling was chosen because with a reasonable preload, the coupling can achieve reasonable high stiffness, such that the resonant frequency of the platform will be approach being limited by the stiffness of the actuators themselves. steel V-blocks that are bolted to the sample plate. A kinematic coupling was chosen because with a reasonable preload, the coupling can achieve reasonable high stiffness, such that the resonant

The actuator-sensor feedback loop takes care of any fine motion necessary, but there is still a coarse, one-time adjustment that must occur at the beginning of the measurement in order to bring the sample up towards the cavity. This mechanism is attached to the sample plate and it is what the sample is fixed to. The purpose of this mechanism is to bring the sample up to within 15 microns of the sample, after which the P-753 actuators (ROM of 25 microns) can do the fine positioning. This mechanism is used for a one-time adjustment at the beginning of the measurement. Since it is directly in the metrology loop, any drift in this mechanism will be uncompensated by the actuator-sensor feedback loop and will directly contribute to drift in the separation during the course of the measurement. Therefore, the coarse z-adjustment mechanism must satisfy the following criteria:

- It must be very stable- minimal sliding, drifting, or expanding during a measurement. The dimensional instability of this mechanism will directly contribute to the drift during the measurement, so the mechanism must be stable in the z direction with a maximum drift of 1 nm / min in order to meet the overall stability goals for the whole system.
- It must have a range of motion on the order of 0.5 – 1.0 mm
- It must fit in a cylinder with a radius of 3 cm and a height of ~1 – 2 cm

At the heart of the sample positioning system is an active feedback loop for maintaining the

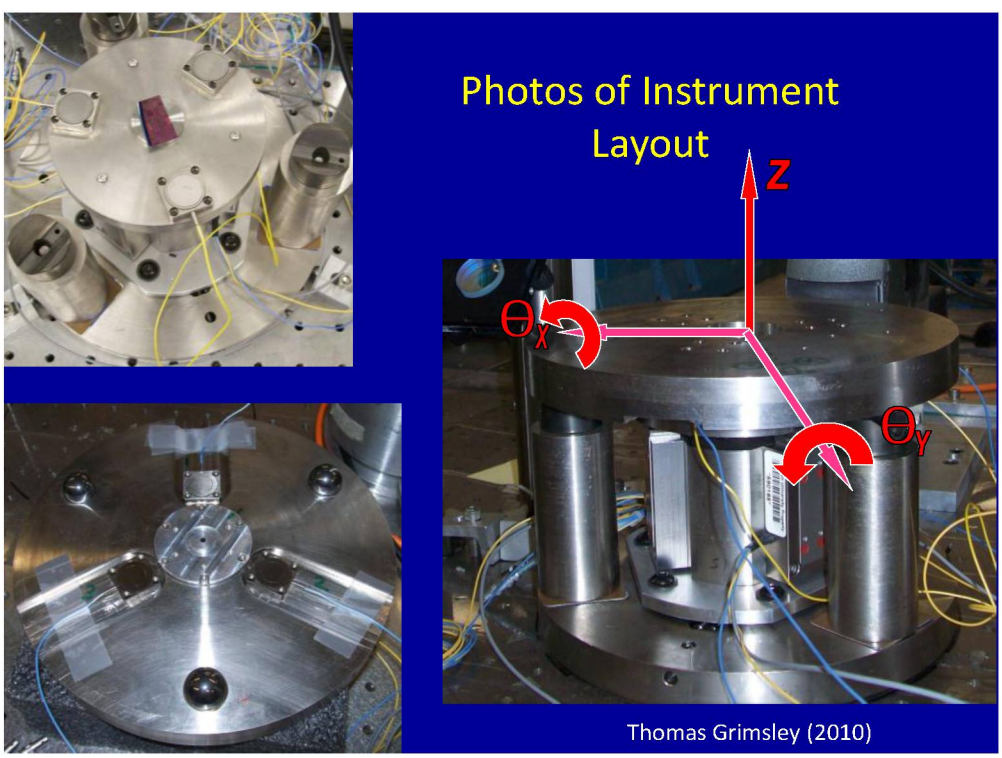

*Figure 3: Photograph of the first prototype instrument from different angles of view. separation between the sample and the cavity. Three piezoelectric actuators (P-753) and three capacitive displacement sensors (D-100 with invar bodies) and a digital controller (E-710) have been purchased from Physik Instrumente Ghmb.*

The kinematic components for the cavity platform (coupling the cavity plate to the posts) and the sample platform (coupling the sample plate to the base) were acquired from Ball-Tec, a company that specializes in making highly spherical balls and also other components for exact constraint design. After machining the invar and non-invar elements the first prototype was completed during this grant year, illustrated by photographs in *Figure 3*. Its stability and precision in terms of the z-stability (distance between the optoacoustic transceiver element and the target material

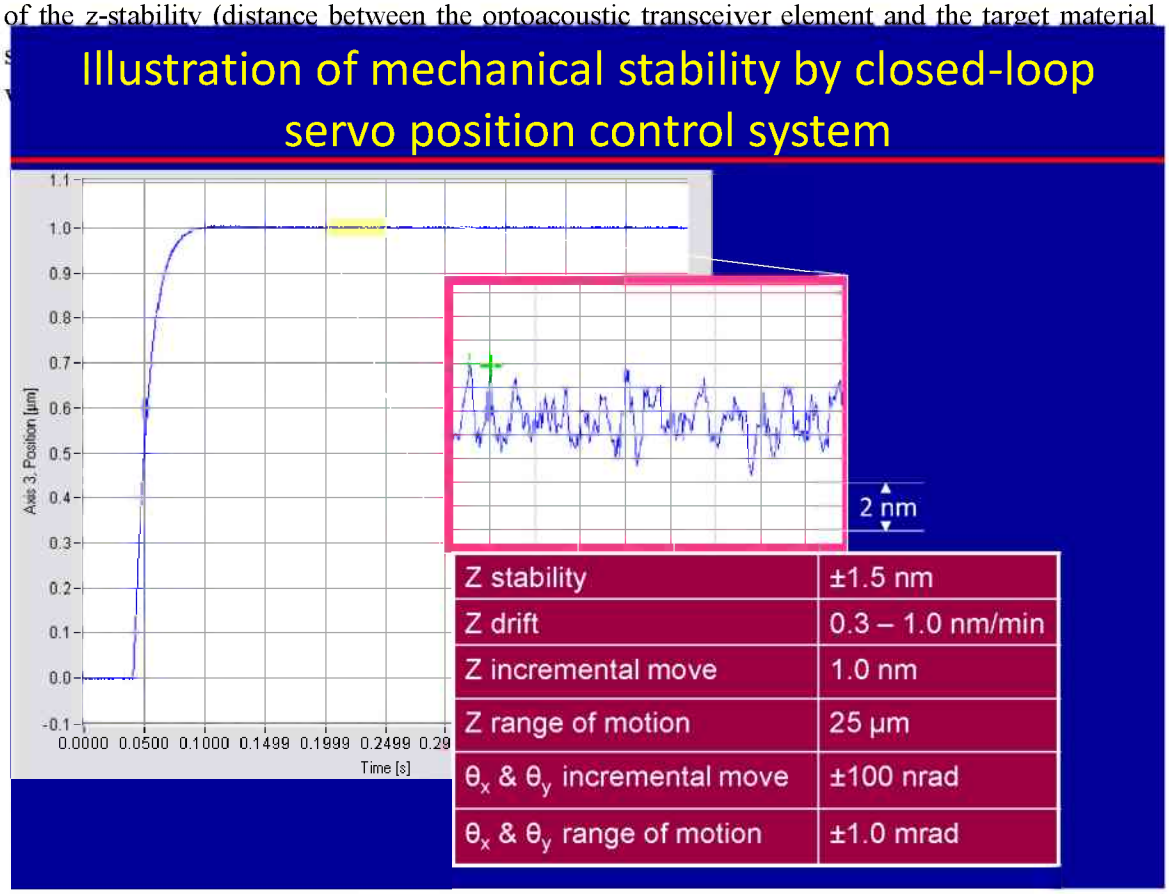


*Figure 4: Stability as a figure of merit of the precision acoustic microscope stage unit assembly. Horizontal axis is in units of time (seconds to minutes) appropriate for taking measurements in a realistic system.*

***Simulation of sound propagation in confined nanostructures***

Both for the design and, especially, in developing numerical algorithms to interpret the metrology outcomes of the POAM, we developed a set of new computational tools. Two simulation methods for modeling the behavior of sound waves in a viscid and compressible fluid are presented next. First, a finite difference time domain (FDTD) method for modeling the scattering of sound from rigid nanostructures is demonstrated. The, a frequency domain treatment of the problem of a fluid in an infinite channel waveguide is presented, and a numerical technique for determining the

phase velocity and attenuation of the propagating modes is demonstrated. Both of these simulation methods, especially the FDTD program were used to interpret the POAM experimental results.

***Simulation of the scattering of sound from periodic nanostructures***

In a POAM measurement, the lateral extent of the sound launched into the coupling fluid is determined by the excitation area, *i.e.*, the focused spot size of the laser. For the optical setup used in this work, the excitation area was a circle with a radius of 10 – 15 μm. The large excitation area rules out the possibility of resolving individual nanostructures without further focusing of the sound. However, by examining a periodic array of structures with submicron

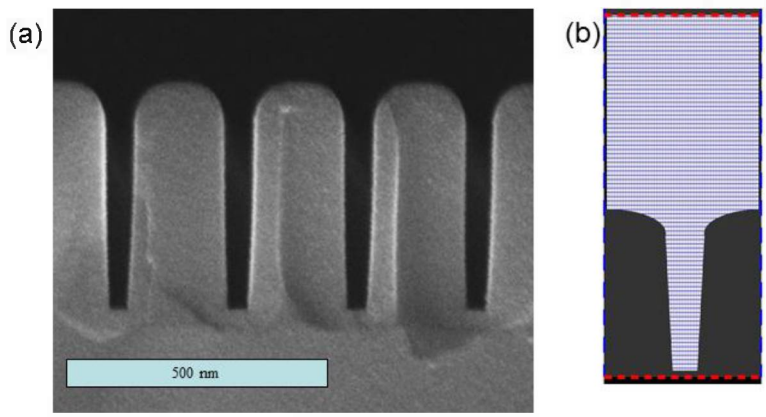


*Figure 5: (a) Cross sectional SEM image of a typical sample studied in this work. Scale bar is 500 nm (b) Schematic of the computational domain. Zero displacement boundary conditions were enforced on the top and bottom faces (red dashed lines), and periodic boundary conditions were enforced on the lateral boundaries (blue dashed lines). The solid (gray) was taken to be a fluid with a density $10^6$ times larger than that of water.*

features, average properties of the structures can be measured. Figure 5a shows a cross sectional scanning electron microscope (SEM) image of one of the samples studied. The samples were periodic in 1 dimension, and the spatial repeat distance, or period, of the sample was between 250 – 500 nm. Given the size of the excitation area, approximately 20 – 40 nanostructures were probed during a single measurement. More details about the nanostructure sample fabrication will be given below.

The linearized partial differential equations describing the motion of the fluid are the continuity equation

$$\frac{1}{\rho_0}\frac{\partial \rho}{\partial t} + \vec{\nabla}\cdot\mathbf{v} = 0, \qquad 1.1$$

where $\rho_0$ is the density of the fluid in the absence of any sound and $\mathbf{v}$ is the velocity field, and Newton's second law applied to a fluid element

$$\rho_0 \frac{\partial \mathbf{v}}{\partial t} = \vec{\nabla}\cdot\mathbf{P}. \qquad 1.2$$

The connection between the density and the pressure is

$$B_s = \left( \rho \frac{\partial P}{\partial \rho} \right)_s , \qquad 1.3$$

where $B_s$ is the bulk isentropic compressibility and is taken to be a constant. The divergence of the stress tensor can be written as[1]

$$\vec{\nabla} \cdot \mathbf{P} = -\nabla P + \vec{\nabla} \cdot \left( \mathbf{P}' + \mathbf{P}'' \right), \qquad 1.4$$

where $P$ is the hydrostatic pressure, and

$$P_{ij}' = \eta \left( \frac{\partial v_i}{\partial x_j} + \frac{\partial v_j}{\partial x_i} \right); P_{ii}' = 2\eta \left( \frac{\partial v_i}{\partial x_i} - \frac{\vec{\nabla} \cdot \mathbf{v}}{3} \right), \qquad 1.5$$

and

$$P_{ij}'' = 0; P_{ii}'' = \zeta \left( \vec{\nabla} \cdot \mathbf{v} \right). \qquad 1.6$$

The quantities $\eta$ and $\zeta$ are the shear and volume coefficients of viscosity of the fluid. The second coefficient of viscosity can be deduced from measurements of the acoustic attenuation. It is straightforward to show, that for plane acoustic waves of the form

$$p(z,t) = p_0 \exp(-\alpha z) \exp\left[ i \left( kz - \omega t \right) \right], \qquad 1.7$$

where $p$ is the excess pressure, that

$$\alpha = \frac{\omega^2}{2c_0^3 \rho_0} \left( \frac{4}{3}\eta + \zeta \right), \qquad \omega = kc_0, \qquad 1.8$$

provided that $\alpha << k$, where $c_0 = \left( B_s / \rho_0 \right)^{1/2}$ is the low frequency sound velocity. From the measured acoustic attenuation the volume coefficient of viscosity can be calculated. The relevant properties of water at 22 °C needed for the simulations are summarized in Table I.

| $\rho_0$ $\left(g \cdot cm^{-3}\right)$ | $c_0$ $\left(cm \cdot s^{-1}\right)$ | $A$ $\left(s^2 \cdot cm^{-1}\right)$ | $\eta$ $\left(g \cdot s^{-1} \cdot cm^{-1}\right)$ | $\left(\zeta / \eta\right)$ |
|---|---|---|---|---|
| 0.9977 | $1.4876 \times 10^5$ | $2.39 \times 10^{-17}$ | $9.62 \times 10^{-3}$ | 2.81 |

Table I: Density, sound velocity, shear viscosity, and the ratio of bulk to shear viscosity for water at a temperature of 22 Celsius.

***Finite difference time domain simulations in 2D***

The equations of motion for the fluid in two dimensions, say $x$ and $y$, can be written as

$$\frac{1}{\rho_0 c_0^2} \frac{\partial P}{\partial t} + \frac{\partial v_x}{\partial x} + \frac{\partial v_y}{\partial y} = 0 \qquad 1.9a$$

$$\rho_0 \frac{\partial v_x}{\partial t} = -\frac{\partial P}{\partial x} + \left( \zeta + \frac{\eta}{3} \right) \frac{\partial}{\partial x} \left( \frac{\partial v_x}{\partial x} + \frac{\partial v_y}{\partial y} \right) + \eta \left( \frac{\partial^2 v_x}{\partial x^2} + \frac{\partial^2 v_x}{\partial y^2} \right), \qquad 1.9b$$

$$\rho_0 \frac{\partial v_y}{\partial t} = -\frac{\partial P}{\partial y} + \left( \zeta + \frac{\eta}{3} \right) \frac{\partial}{\partial y} \left( \frac{\partial v_x}{\partial x} + \frac{\partial v_y}{\partial y} \right) + \eta \left( \frac{\partial^2 v_y}{\partial x^2} + \frac{\partial^2 v_y}{\partial y^2} \right). \qquad 1.9c$$

A finite difference time domain (FDTD) method was used to simulate the scattering of a sound pulse off of a periodic rigid structure. Figure 5b shows a schematic of the computational domain. The domain was split into a grid. The particle acceleration, velocity, and displacement were calculated on the grid points, while the strain and stress were computed in the center of the square formed by four grid points. Periodic boundary conditions were applied in the $x$ direction, and the top and bottom faces were held fixed. To simulate the incoming pulse generated by the cavity, the top face was displaced by a distance of 10% of the grid spacing, and was then held at that position for subsequent time steps. In the simulation, the rigid solid structure was modeled as a fluid with the same properties as water but with a density $10^6$ times larger than that of water. After each time step, the average pressure on the boundary was recorded.

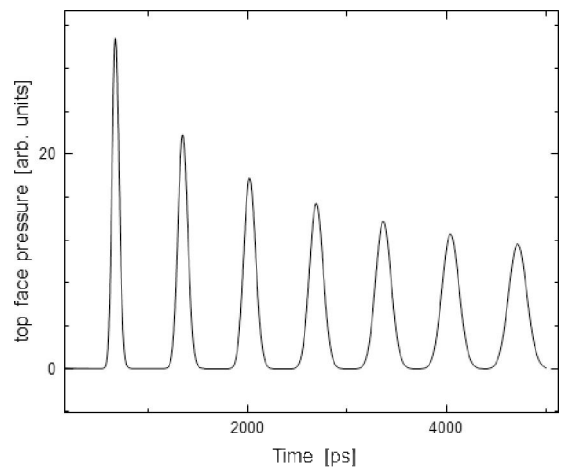


*Figure 6: Simulation results for a water gap of 505 nm. The average pressure on the top face is shown above. The mesh size was 5 nm and the time step was 2 ps.*

As a test, no solid was included in the domain, and the initial pulse was allowed to traverse the water gap several times. The mesh size was 5 nm and the time step 1 ps. All of the fluid properties used in the simulation were the same as those in Table I, except the sound velocity was rounded up to 1.5 nm $ps^{-1}$. The period was 400 nm, and the distance from the top boundary to the bottom was 505 nm. The average pressure on the top face versus time is shown in Fig. 6. The expected solution is a series of echoes of the form

$$s(t) = \sum_n \frac{a_1}{\sqrt{n}} \exp\left[ -\left( \frac{t - nt_0}{\sigma_0 \sqrt{n}} \right)^2 \right], \qquad 1.10$$

where $a_1$ is the amplitude of the first echo. The arrival time of the first echo is

$$t_0 = 2d / c_0, \qquad 1.11$$

and the width of the first echo, from Eq. 1.8

$$\sigma_0 = \sqrt{\frac{2}{c_0^3 \rho_0} \left( \frac{4}{3}\eta + \zeta \right) (2d)} \ . \qquad 1.12$$

For the data in Fig. 6, a Gaussian of the form

$$a_n \exp\left[-\left(\frac{t-t_n}{\sigma_n}\right)^2\right], \qquad 1.13$$

was fitted to each echo, and the results are shown in Table II. For the parameters used, the expected value of $t_0$ is 673.33 ps and that of $\sigma_0$ is 48.90 ps. The simulation results agree quite well with the expected result. The above was repeated for several mesh sizes and time steps, and similar results were obtained.

| Echo number (n) | $(a_n/a_1)$ | $t_n$ [ps] | $(t_n - t_{n-1})$ [ps] | $\sigma_n$ [ps] | $\left(\frac{\sigma_n - \sqrt{n}\sigma_0}{\sqrt{n}\sigma_0}\right)$ [ % ] | $(a_n/a_1)^{-2}$ |
|---|---|---|---|---|---|---|
| 1 | 1 | 673.338 | | 48.936 | 0.075 | 1 |
| 2 | 0.7076 | 1346.467 | 673.130 | 69.168 | 0.020 | 2.00 |
| 3 | 0.5779 | 2019.803 | 673.336 | 84.695 | -0.001 | 2.99 |
| 4 | 0.5006 | 2693.138 | 673.335 | 97.789 | -0.010 | 3.99 |
| 5 | 0.4477 | 3366.471 | 673.334 | 109.329 | -0.012 | 4.99 |
| 6 | 0.4088 | 4039.809 | 673.338 | 119.753 | -0.020 | 5.98 |
| 7 | 0.3785 | 4713.140 | 673.331 | 129.344 | -0.024 | 6.98 |

Table II: Results of fitting a Gaussian of the form Eq. 1.13 to each of the echoes.

Table III summarizes the approximate maximum time step for which the algorithm is stable for a given mesh size, as well as the time step used for simulation results presented in this work.

| mesh nm | approximate maximum time step ps | time step used Ps |
|---|---|---|
| 10 | 5 | 4 |
| 5 | 2 | 1 |
| 2 | 0.4 | 0.25 |
| 1 | 0.1 | 0.1 |

Table III: Time steps used for mesh sizes used in this work. For time steps larger than approximate maximum time step, the algorithm became unstable.

***Simulation of the propagation of sound in a channel with fixed slip length***

Structures of the form shown in Fig. 5 can serve as sensitive test for the presence of slip between the water and the sidewalls of the channels, since as the sound pulse incident on the structure gets funneled into the channel, appreciable strain-rates at the solid-liquid boundary can be expected. The simulation program described above effectively enforces a no-slip boundary condition at the

solid-liquid interfaces. One way to include slip at the boundary would be to add a layer of fluid with low viscosity at the solid-liquid interface. This model of the solid-liquid interface has at least two adjustable parameters: the thickness of the boundary layer and the factor by which the viscosities are reduced. A related problem, with only one adjustable parameter, was considered to gain some insight on the effect of slip on sound propagating down a nanoscale channel.

One way to treat slip at the solid-liquid interface is through the implementation of the boundary condition, first proposed by Navier[2], where the tangential velocity of the fluid along the interface, $v_t$, is proportional to the shear strain rate at the surface

$$v_t = b\left(\nabla v_t \cdot \mathbf{n}\right), \qquad 1.14$$

where $\mathbf{n}$ is a unit vector which points from the solid into the liquid and is normal to the interface. The quantity $b$ has dimensions of length and is called the slip length. Geometrically this is the distance into the wall at which the velocity $v_t$ extrapolates to 0, as shown in Fig. 7a. At this point, no mention will be made as to proposed mechanisms of slip; in this section, the mathematical problem stated below is treated.

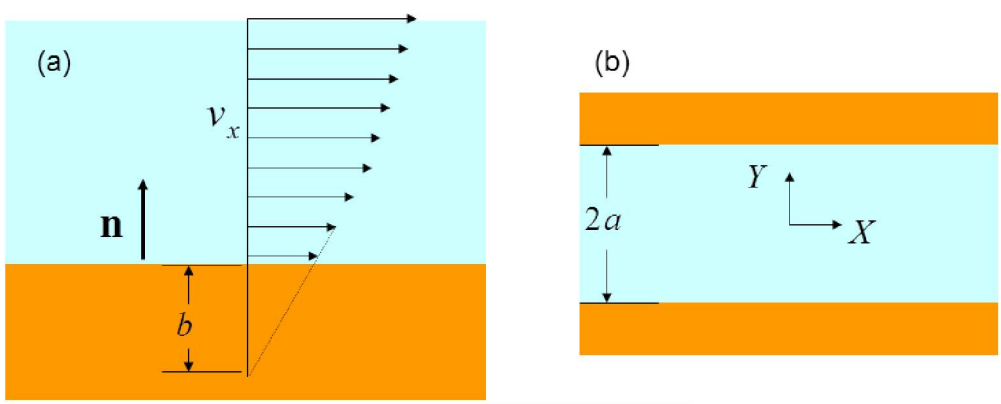


*Figure 7: (a) Definition of the slip length. (b) The geometry of the problem considered was an infinite channel with a width of 2a, and at the rigid walls either a no slip or a fixed slip length boundary condition was enforced.*

The geometry of the problem is shown in Fig. 7b. The fluid extends to infinity in the $x$ and $z$ directions, and is bounded by two impenetrable walls at $y = a$ and $y = -a$. Solutions of Eqs. 1.9a-c of the form $\exp\left[i\left(kx-\omega t\right)\right]$ are sought for the cases of (1) no slip and (2) slip characterized by slip length $b$ at the boundaries. By considering the effect of the slip length on the phase velocity and attenuation of various frequency components as they propagate down the channel, some insight as to the magnitude of the effects of slip can be gained. The starting point is the treatment of Sorokin and Chubinskij [3], who used velocity potentials to find the dispersion relation for the no slip case. The same method is applied to the slip boundary condition case, and the roots of the dispersion relation were found numerically.

***Infinite channel with no-slip boundary conditions***

Equations 5.9 can be written in the form

$$\frac{\partial s}{\partial t} = -\frac{\partial v_x}{\partial x} - \frac{\partial v_y}{\partial y}, \qquad 1.15a$$

$$\frac{\partial v_x}{\partial t} = -A\frac{\partial s}{\partial x} + (B+C)\frac{\partial^2 v_x}{\partial x^2} + B\frac{\partial^2 v_x}{\partial y^2} + C\frac{\partial^2 v_y}{\partial x \partial y}, \qquad 1.15b$$

$$\frac{\partial v_y}{\partial t} = -A\frac{\partial s}{\partial y} + B\frac{\partial^2 v_y}{\partial x^2} + (B+C)\frac{\partial^2 v_y}{\partial y^2} + C\frac{\partial^2 v_x}{\partial x \partial y}, \qquad 1.15c$$

where $s$ is the fractional change in density

$$s = \frac{\rho - \rho_0}{\rho_0}. \qquad 1.16$$

The constants $A$, $B$, and $C$ are

$$A = c_0^2,\ B = \left(\frac{\eta}{\rho_o}\right),\ \text{and}\ C = \left(\frac{\frac{1}{3}\eta + \zeta}{\rho_o}\right). \qquad 1.17$$

The fluid velocity can be expressed in terms of a scalar and vector potential

$$\mathbf{v} = \vec{\nabla}\phi + \vec{\nabla} \times \mathbf{\Psi}. \qquad 1.18$$

In this problem, the only non-zero component of the vector potential is the $z$ component, and the vector potential can be written as

$$\mathbf{\Psi} = \psi(x, y)\hat{\mathbf{e}}_z. \qquad 1.19$$

The $x$ and $y$ components of the velocity, in terms of the potentials, are

$$v_x = \frac{\partial \phi}{\partial x} + \frac{\partial \psi}{\partial y},\ v_y = \frac{\partial \phi}{\partial y} - \frac{\partial \psi}{\partial x}. \qquad 1.20$$

Substituting the above into Eq. 1.15 yields two equations for the two potentials

$$\frac{\partial}{\partial t}\psi = B\left(\frac{\partial^2}{\partial x^2} + \frac{\partial^2}{\partial y^2}\right)\psi, \qquad 1.21a$$

$$\frac{\partial^2 \phi}{\partial t^2} = \left[(B+C)\frac{\partial}{\partial t} + A\right]\left(\frac{\partial^2 \phi}{\partial x^2} + \frac{\partial^2 \phi}{\partial y^2}\right). \qquad 1.21b$$

The use of velocity potentials has simplified the partial differential equations, but at the cost of complicating the boundary conditions. A no-slip boundary condition was enforced at the edges of the waveguide

$$v_x(x, y = \pm a) = 0, \qquad 1.22$$

and no fluid was allowed to penetrate the wall

$$v_y(x, y = \pm a) = 0 . \qquad 1.23$$

Solutions for the potentials of the form

$$\phi(x, y) = g(y)\exp\left[i(kx - \omega t)\right], \qquad 1.24a$$

$$\psi(x, y) = h(y)\exp\left[i(kx - \omega t)\right]. \qquad 1.24b$$

are sought. The boundary conditions, using 1.24, become

$$ikg(y = \pm a) + h'(y = \pm a) = 0, \qquad 1.25a$$

$$g'(y = \pm a) - ikh(y = \pm a) = 0 . \qquad 1.25b$$

Substituting Eq. 1.24 into Eq. 1.21 yields two ordinary differential equations

$$h''(y) = \left(-i\frac{\omega}{B} + k^2\right)h(y), \qquad 1.26$$

$$g''(y) = \left(-\frac{A\omega^2 + i\omega^3(B + C)}{A^2 + \omega^2(B + C)^2} + k^2\right)g(y). \qquad 1.27$$

Through the change of variables $\tilde{y} = y/a$ and the introduction of the dimensionless parameters for the wave number and the angular frequency $K = ka$, $\Omega = \omega a / c_o$, and the dimensionless parameters

$$\gamma = \frac{B}{c_0 a}, \ \mu = \frac{(B + C)}{c_0 a}, \qquad 1.28$$

equations 1.26 and 1.27 become

$$g''(\tilde{y}) = \left(K^2 - \frac{\Omega^2 + i\mu\Omega^3}{1 + \mu^2\Omega^2}\right)g(\tilde{y}), \qquad 1.29$$

$$h''(\tilde{y}) = \left(K^2 - i\frac{\Omega}{\gamma}\right)h(\tilde{y}). \qquad 1.30$$

The solutions to the above are

$$h(\tilde{y}) = A_1\cos\beta\tilde{y} + A_2\sin\beta\tilde{y}, \qquad 1.31a$$

$$g(\tilde{y}) = B_1\cos\alpha\tilde{y} + B_2\sin\alpha\tilde{y}, \qquad 1.31b$$

where

$$\beta = \sqrt{i\frac{\Omega}{\gamma} - K^2}, \ \alpha = \sqrt{\frac{\Omega^2 + i\mu\Omega^3}{1 + \mu^2\Omega^2} - K^2} . \qquad 1.32$$

Substituting Eq. 1.31 into the boundary conditions yields four equations

$$\begin{pmatrix} 0 & \beta\cos\beta & iK\cos\alpha & 0 \\ -\beta\sin\beta & 0 & 0 & iK\sin\alpha \\ -iK\cos\beta & 0 & 0 & \alpha\cos\alpha \\ 0 & iK\sin\beta & \alpha\sin\alpha & 0 \end{pmatrix}\begin{pmatrix} A_1 \\ A_2 \\ B_1 \\ B_2 \end{pmatrix} = 0. \qquad 1.33$$

The above is a homogenous linear system of equations for the coefficients $A_1$, $A_2$, $B_1$, and $B_2$. A sufficient and necessary condition for a solution to exist is that the determinant of the coefficient matrix vanishes. The determinant of the coefficient matrix in Eq. 1.33 can be expressed as the product of two quantities

$$\left(\alpha\beta\cos\alpha\sin\beta + K^2\sin\alpha\cos\beta\right)\left(\alpha\beta\sin\alpha\cos\beta + K^2\cos\alpha\sin\beta\right) = 0. \qquad 1.34$$

This implies that either

$$\left(\alpha\beta\cos\alpha\sin\beta + K^2\sin\alpha\cos\beta\right) = 0, \qquad 1.35a$$

or

$$\left(\alpha\beta\sin\alpha\cos\beta + K^2\cos\alpha\sin\beta\right) = 0. \qquad 1.35b$$

Equations 1.35a and 135b are dispersion equations and express the relationship between the dimensionless frequency $\Omega$ and wave number $K$. From Eqs. 1.33 and 1.31 it can be shown that Eq. 1.35a corresponds to $A_1 = B_2 = 0$. The first dispersion relation applies to modes where the potential $\phi$ has even symmetry about the center of the waveguide. Likewise, it can be shown that the second dispersion relation corresponds to modes where $A_2 = B_1 = 0$, which are modes where the potential $\phi$ has odd symmetry.

***Infinite channel with slip length boundary conditions***

The above analysis can be repeated using a slip boundary condition. Applying the boundary condition of Eq. 1.14 to this geometry

$$v_x(x,a) = -b\left.\frac{\partial v_x}{\partial y}\right|_{y=a}, \text{ and } v_x(x,-a) = b\left.\frac{\partial v_x}{\partial y}\right|_{y=-a}. \qquad 1.36$$

The boundary condition on the normal component ( $v_y$ ) of the fluid velocity is still Eq. 1.23 for the no slip case.

By introducing the dimensionless slip parameter $\lambda = b/a$, the boundary conditions become

$$iKg(\tilde{y}=1) + h'(\tilde{y}=1) = -i\lambda Kg'(\tilde{y}=1) + \lambda\beta^2 h(\tilde{y}=1), \qquad 1.37$$

$$iKg(\tilde{y}=-1) + h'(\tilde{y}=-1) = i\lambda Kg'(\tilde{y}=-1) - \lambda\beta^2 h(\tilde{y}=-1), \qquad 1.38$$

$$g'(\tilde{y}=\pm 1) - iKh(\tilde{y}=\pm 1) = 0. \qquad 1.39$$

Proceeding in the same way as before yields four equations for the coefficients in Eq. 1.31, which now become

$$\begin{pmatrix} 0 & \beta\cos\beta-\lambda\beta^2\sin\beta & iK\cos\alpha-i\lambda K\alpha\sin\alpha & 0 \\ -\beta\sin\beta-\lambda\beta^2\cos\beta & 0 & 0 & iK\sin\alpha+i\lambda K\alpha\cos\alpha \\ -iK\cos\beta & 0 & 0 & \alpha\cos\alpha \\ 0 & iK\sin\beta & \alpha\sin\alpha & 0 \end{pmatrix}\begin{pmatrix} A_1 \\ A_2 \\ B_1 \\ B_2 \end{pmatrix}=0$$

. 1.40

This results in two dispersion relations, one for modes where $\phi$ has even symmetry

$$\left(\alpha\beta\cos\beta\sin\alpha+K^2\cos\alpha\sin\beta\right)-\lambda\alpha\left(\beta^2+K^2\right)\sin\beta\sin\alpha=0, \qquad 1.41a$$

and one where $\phi$ has odd symmetry

$$\left(K^2\sin\alpha\cos\beta+\beta\alpha\sin\beta\cos\alpha\right)+\lambda\alpha\left(\beta^2+K^2\right)\cos\beta\cos\alpha=0. \qquad 1.41b$$

As λ approaches 0, the no-slip dispersion relations are recovered. Using the above results, the expressions for $v_x$ and $v_y$ for the even symmetry modes become

$$v_x(x,y)=\frac{A_2}{a}\left[\cos\left(\alpha\frac{y}{a}\right)\left(\lambda K^2\frac{\sin\beta}{\cos\alpha}+\lambda\beta^2\frac{\sin\beta}{\cos\alpha}-\beta\frac{\cos\beta}{\cos\alpha}\right)+\beta\cos\left(\beta\frac{y}{a}\right)\right]\exp\left[i\left(kx-\omega t\right)\right]+c.c.$$

$$v_y(x,y)=\frac{A_2}{a}\left[iK\frac{\sin\beta}{\sin\alpha}\sin\left(\alpha\frac{y}{a}\right)-iK\sin\left(\beta\frac{y}{a}\right)\right]\exp\left[i\left(kx-\omega t\right)\right]+c.c.$$

1.42

***Numerical determination of the phase velocity and attenuation***

The dispersion relations in Eq. 1.41 cannot be expressed as a simple function such as $K(\Omega)$ for either the slip or no-slip case, and to make progress we must resort to a numerical approach. For a given channel width and fluid properties, Eq. 1.41 becomes a complex transcendental equation of the form $f(K,\Omega)=0$. The goal is to find the roots $K$ of this equation for a given value of the dimensionless frequency $\Omega$. The frequency is restricted to be real and positive. For each $\Omega$, there will be a series of complex $K$ that satisfy the dispersion relation. Each root $K$ will belong to a particular mode. The search for roots is restricted to $\mathrm{Re}(K)\geq 0$ and $\mathrm{Im}(K)\geq 0$. From Eq. 1.24, these restrictions on the real and imaginary parts of $K$ correspond to damped waves traveling in the positive $x$ direction.

Assuming a root $K$ for a value of $\Omega$ has been found, the phase velocity is

$$c_{phase}=c_0\frac{\Omega}{\mathrm{Re}(K)}, \qquad 1.43$$

and the amplitude attenuation is given by

$$\delta = \frac{\mathrm{Im}(K)}{a}, \qquad 1.44$$

such that after propagating a distance $D$, the wave amplitude will be diminished by a factor $\exp(-\delta D)$.

The roots $K$ for a given value of $\Omega$ were found by implementing a simplified version of what is referred to as the direct Kuhn algorithm[4]. The technique is derived from the related problem of finding the roots of a complex polynomial

$$f(z) = \sum_{n=0}^{N} a_n z^n, \qquad 1.45$$

where the coefficients $a_n$ are constant and complex. For complex polynomials of the form of Eq. 1.45, Kuhn observed that the search for the roots, *i.e.*, the $N$ values of $z$ such that $f(z) = 0$, can be implemented in the following way[5]. The complex plane is divided into a grid, and the function $f$ is evaluated at each point. A label is then given to each point based on the rule

$$L(z) = \begin{cases} 0 & -\pi/3 < \arg[f(z)] \le \pi/3 \\ 1 & \arg[f(z)] > \pi/3 \\ 2 & \arg[f(z)] \le -\pi/3 \end{cases}. \qquad 1.46$$

Kuhn was able to show that if a triangle in the complex plane formed by the points $z_1$, $z_2$, $z_3$ has one of each label, then at least one root is located in that triangle. Various algorithms have been written that involve searching for triangles with roots in them and then subdividing those triangles and repeating the process[5,6]. The rigorous proof that the above method will converge onto the roots of $f$ is based on the assumption that the function is a polynomial. However, it has been demonstrated that the above procedure will converge onto roots of the function even if it is not a polynomial. Long and Jiang[4] showed empirically for several examples that as long as the function is not varying too rapidly in the neighborhood around a root, then the above procedure will still converge onto the root. Intuitively, if the function $f$ is well behaved near its root, then it can replaced by its polynomial approximation.

In the implementation used in this work, the domain of $K$ space being searched was split into a square grid. The program scanned along the boundary of the domain until it found two adjacent points with different labels, and then walked into the domain until it found a square whose four corners had all three labels; this is illustrated in Figure 8. That particular square was then subdivided into a smaller grid, and the procedure was repeated. The label was found using the

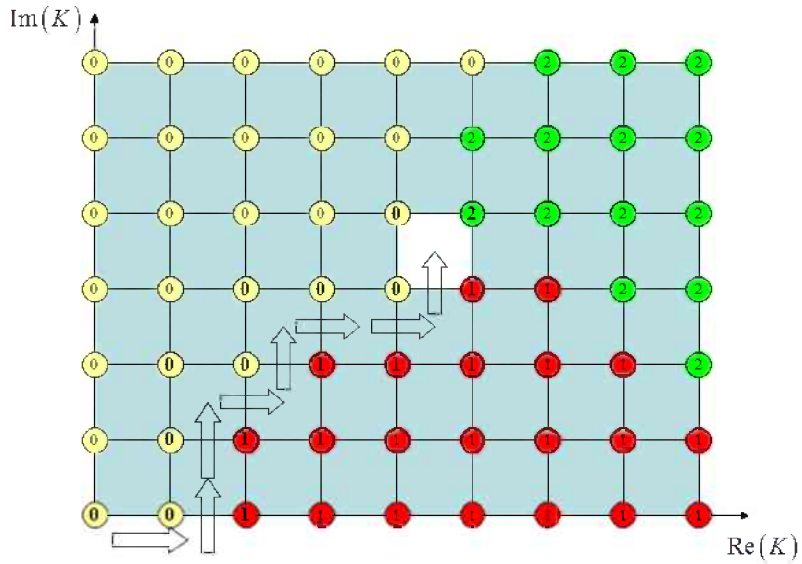


*Figure 8: Implementation of the direct Kuhn algorithm on a square grid. The program walks along the bottom boundary of the domain being searched until it finds two adjacent points with different labels. The program then walks into the domain, progressing from square to square along the boundary between the regions with different labels, until it finds the square where at least one of each label is present. That square is then divided into a smaller grid, and the search is repeated. The bold labels are represent the points where f(K) is evaluated.*

rule in Eq. 1.46, where $f$ is the left hand side of the dispersion relation Eq. 1.41a. Note that this method does not require the function $f$ to be evaluated at every point in the domain.

As an illustration, consider a channel with half width a = 25 nm. Using the above procedure, the values of K that satisfy the dispersion relation Eq. 1.41a for a frequency of 1 GHz for the no slip case (b = 0 nm) and a small slip case (b = 5 nm ) were found . The values of the various dimensionless parameters are summarized in Table IV for the two cases considered here.

| case | $a$ | $b$ | $f$ | $\Omega$ | $M$ | $\gamma$ | $\lambda$ |
|---|---|---|---|---|---|---|---|
| 1 | 25 nm | 0 nm | 1 GHz | 0.10472 | 0.0259 | 0.107 | 0.0 |
| 2 | 25 nm | 5 nm | 1 GHz | 0.10472 | 0.0259 | 0.107 | 0.2 |

Table IV: Parameters used for the two cases considered here.

Figure 9a shows the label at all the points in the domain Re $K$ < 10, Im $K$ <10 for case 1 (no slip). This is shown for the purpose of illustrating the locations of the various roots in the domain; the above described search algorithm does not actually label all of the points in the domain being searched. From this, it appears that there are at least 4 roots in this domain, labeled $S_n$, $n = 0, \ldots 3$ ($S$ stands for symmetric.) Even though the function is transcendental, the program rapidly converged on all the roots. Figure 10 shows a close up of the region of $K$ space around roots $S_0$ and $S_1$ for case 1. The contours represent lines of constant $f(K)$. The algorithm has some difficulty around $S_1$; the circled point labeled B is not a root, even though it appears that all 3 labels are present in the circle on the plot. The point A appears to be a root, since the value of

*f(K)* can be made quite small at the point. For some frequencies and values of the channel half-

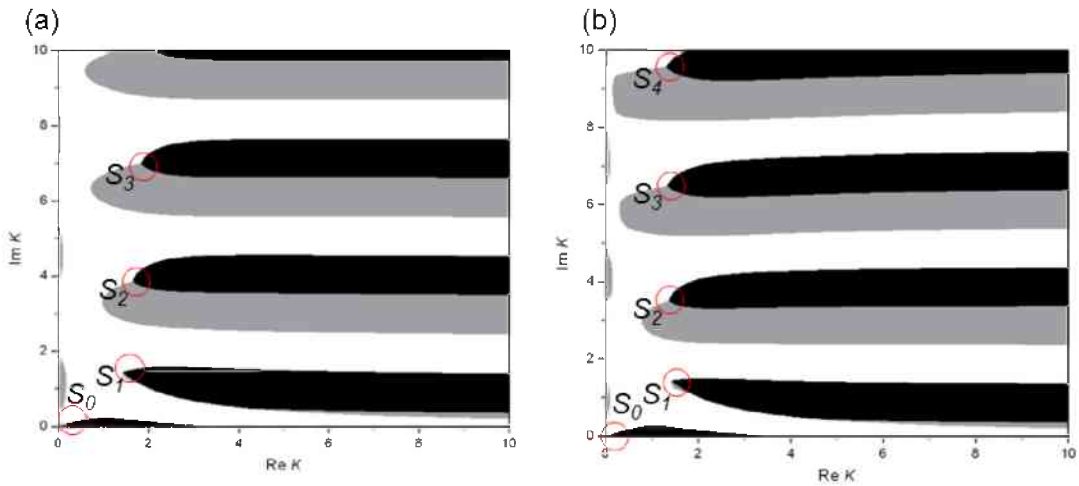


*Figure 9: Fully labeled domain for (a) case 1 and (b) case 2. The roots of the dispersion relaxation are at the points where the domains with labels 0, 1, and 2 intersect.*

width *a*, the algorithm missed the root $S_1$.

Table V shows the roots that the algorithm converged on for case 1 (no slip). The fact that these values of *K* do indeed satisfy the dispersion relation is borne out by the fact that $|f(K)|$ can be made on the order of $10^{-9}$ or less.

| Root | Re *K* | Im *K* | $\lvert f(K)\rvert$ |
|---|---|---|---|
| $S_0$ | 1.19535792E-1 | 3.5761892E-2 | 1.4E-9 |
| $S_1$ | 1.42110075649 | 1.42110075649 | 4.4E-7 |
| $S_2$ | 1.6383275783 | 3.8509426084 | 3.5E-9 |
| $S_3$ | 1.8195935673 | 6.9881904153 | 4.3E-9 |

Table V: Roots converged on by the search algorithm in the domain searched for the case a = 25 nm, b = 0 nm (no slip), and f = 1 GHz.

Figure 9b shows the label at all the points in the domain Re *K* < 10, Im *K* <10 for case 2 (*b* = 5 nm). From this, it appears that there are 5 roots in this domain, and Table VI shows the roots found for case 2 in this domain. In both the slip and no slip cases, all of the modes are strongly damped except for $S_0$.

| Root | Re K | Im K | $\lvert f(K)\rvert$ |
|---|---|---|---|
| $S_0$ | 1.10941325E-1 | 2.433995E-2 | 2.3E-9 |

| | | | |
|---|---|---|---|
| $S_1$ | 1.42110075649 | 1.42110075649 | 7.2E-7 |
| $S_2$ | 1.3722431474 | 3.498781262 | 4.7E-9 |
| $S_3$ | 1.3378452361 | 6.484123250 | 7.2E-9 |
| $S_4$ | 1.3166866661 | 9.5624272427 | 9.7E-9 |

Table VI: Roots converged on by the search algorithm for the case a = 25 nm, b = 5 nm, and f = 1 GHz.

Table VII shows the relative phase velocity and the amplitude attenuation factor after propagating a distance of 100 nm for the roots for cases 1 and 2.

Case 1 ( b = 0 nm) Case 2 (b = 5 nm)

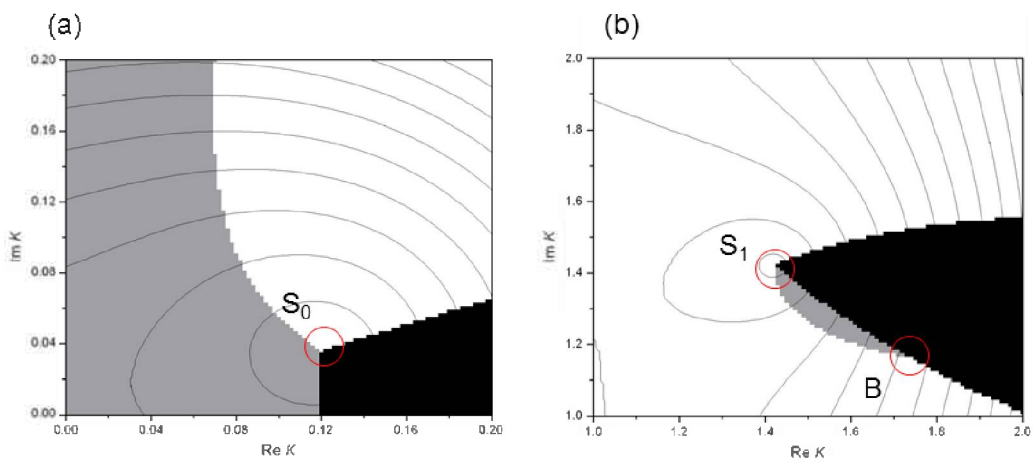


*Figure 10: Fully labeled domains around roots (a) $S_0$ and (b) $S_1$ for case 1. The contours are levels of constant |f(K)|. The point B is not a root.*

| Root | Relative phase velocity (% of $c_0$) | $\exp(-\delta D)$ for $D$ = 100 nm | Relative phase velocity (% of $c_0$) | $\exp(-\delta D)$ for $D$ = 100 nm |
|---|---|---|---|---|
| $S_0$ | 87.6 | 0.867 | 94.5 | 0.906 |
| $S_1$ | 7.4 | 0.0034 | 7.4 | 0.0034 |
| $S_2$ | 6.4 | $<10^{-6}$ | 7.7 | $<10^{-6}$ |
| $S_3$ | 5.8 | $<10^{-6}$ | 7.9 | $<10^{-6}$ |
| $S_4$ | - | - | 8.0 | $<10^{-6}$ |

Table VII: Relative phase velocity and amplitude attenuation after 100 nm, computed using Eq. 1.43 and 1.44, for the roots in Tables V and VI. The most notable change to the mode $S_0$, upon the introduction of a finite slip length, is an increase in the phase velocity.

The most noticeable difference between the slip and no slip case is the difference in the phase velocity of almost 7% for the mode $S_0$.

***Comparative Comments on Modeling***

Two markedly different simulation tools were presented in this chapter. The FDTD program was essential in interpreting the results of POAM experiments. The wave guide problem combined with the FDTD program and experimental results provide a means of placing an upper limit on the slip length for a fluid-solid system. The presence of slip will manifest itself as an increase in the speed at which sound propagates down the channel and returns to the transducer; this increase in speed will appear as a discrepancy between the experimental data and the results of the FDTD simulation, which has essentially no slip. From the magnitude of the time discrepancy and the results of the waveguide simulations presented by our model approach, an estimate of the slip length can be obtained.

***Experimental Results with POAM: Planar Optoacoustic Microscopy of 1D Periodic Nanostructures:***

We focused on the use of planar opto-acoustic microscopy (POAM) with samples that were periodic in one dimension. The samples investigated had dimensions that made their non-destructive characterization either difficult or impossible by existing methods. Three different areas were explored. First, the problem of inferring the major dimensions (pitch, line width, and height) along with the profile details (sidewall angle, roundedness of the tops, etc.) was explored by comparing experimental data to a library of simulations and searching for the best fit. Second, the echo from the bottom for channels that were less than 60 nm wide was compared to simulations. Finally, since the presence of slip between the water and the channel side walls would greatly affect both the amplitude and the arrival time of the echo from the bottom of the channel, the POAM data was used to estimate how much slip was present at the water-sidewall interface.

***Sample description and characterization***

Figure 11 shows the structure of the samples used in this work. The samples were fabricated by Novellus Systems, Inc., and consisted of lithographically defined silicon dioxide lines on a silicon substrate that were covered with a conformal coating of silicon nitride that was approximately 60

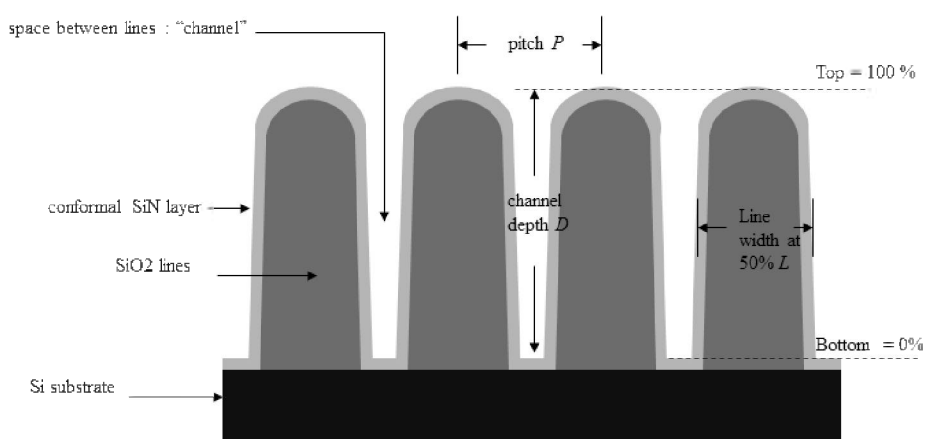


*Figure 11: Cross sectional schematic of the samples studied showing their composition. The line profile was specified by the width of the line (or channel) at various height levels, with 100% corresponding to the tops of the lines.*

nm thick. The gaps between the lines are referred to below as channels. There were two groups of structures; one with channels 400 nm deep, and the other 230 nm deep. There were a variety of patterns on each wafer, and the patterned areas were on the order of 200 μm x 200 μm.

The main features of the structures can be described by three critical dimensions: the repeat distance, or pitch (denoted by *P*), the height of the lines (*D*), and the width of the lines halfway down the channel (*L*). The cross sectional profile of the lines was described by measuring the width of the lines at different heights. The height levels at which the widths of the lines were measured were labeled by a percentage, where 100% corresponded to the top of the line and 0%

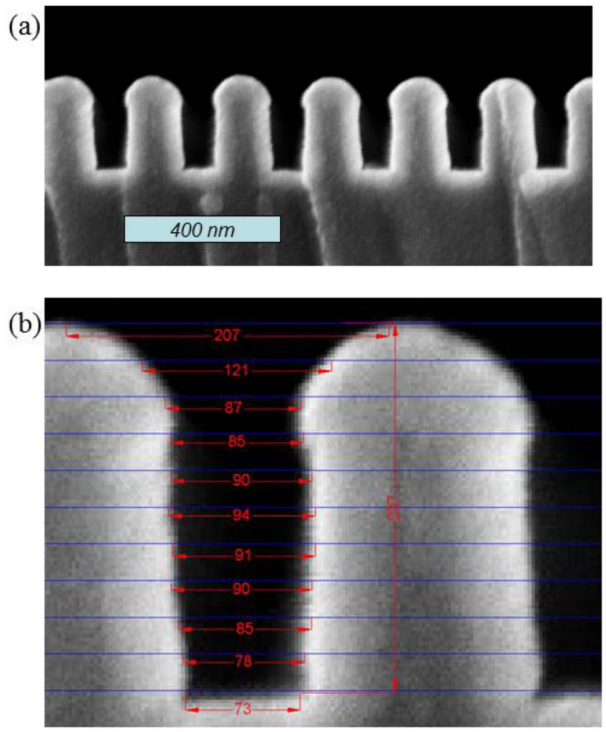


*Figure 12: (a) An example of a cross sectional SEM. Scale bar is 400 nm. (b) A close up view showing the measured widths at 10% height levels. For this image, the uncertainty in the width measurements was +/- 8 nm.*

the bottom of the channel.

The sample profiles were measured by destructive cross sectional scanning electron microscopy (SEM). After each set of POAM measurements, the sample piece was cleaved perpendicular to the lines. The exposed cross section was then coated with approximately 4 nm of evaporated amorphous carbon. The amorphous carbon helped to reduce the effects of surface charging during the imaging process. An example cross sectional SEM image is shown in Figure 12a. The pitch of the structure was 230 ± 5 nm, the channel depth was 235 ± 5 nm, and the line width at 50% was 135 ± 8 nm. A close up view of one of the channels is shown in 12b, with the widths measured at 10% increments of the height. For the highest resolution images, the widths of the lines were measured at height levels of 100% to 90% in 2% increments, and then 85% to 0% in 5% increments. For each of the samples examined in this work, the profiles of 20 – 50 individual

channels were measured. The widths at each height level were then averaged to form the average channel profile that was used in the simulations. In all the simulations, the profile of the line was assumed to be symmetric.

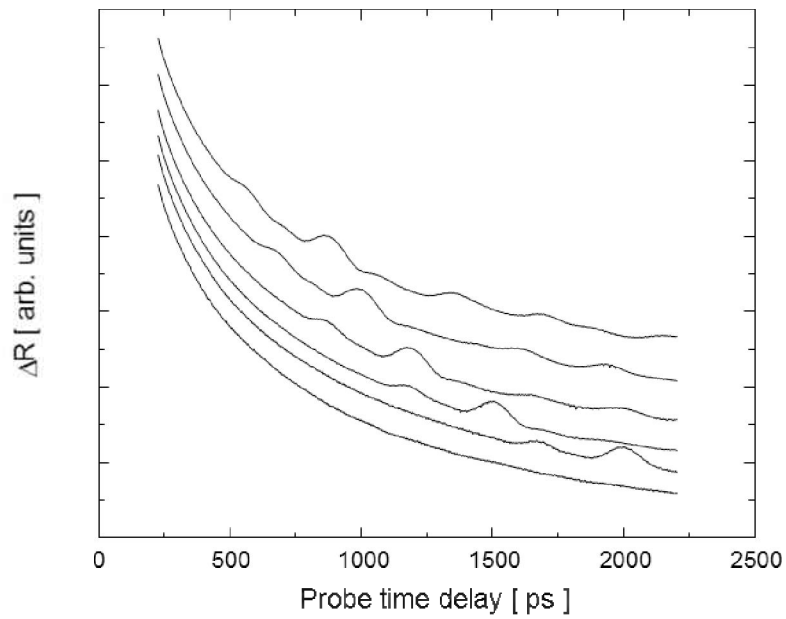


*Figure 13 : POAM data taken at different water film thicknesses for the sample shown in Fig 12.*

***Major features of the POAM data***

The experimental procedure used for acquiring POAM data was as follows: The sample was mounted onto the sample positioning system, one drop of distilled water was placed on the sample, and the cavity was placed on top of the sample. The pump and probe beams were focused onto the cavity transducer, and then the water film thickness was decreased until acoustic echoes were visible in the data. Figure 13 shows the experimental data taken at different water film thicknesses for the sample whose cross sectional image is shown in Figure 12a. The data has been treated as previously described in chapter 4. The lowest curve in Fig. 13 was taken with a water gap at least 0.5 microns larger than the curve above it. A function of the form $y(t) = y_0 + A_1 \exp(-t/\tau_1) + A_2 \exp(-t/\tau_2)$, was fitted to the lowest curve, and $\tau_1$ and $\tau_2$ were found to be 165.0 ps and 842.5 ps, respectively. This background was then subtracted from each data set. Finally, each data set was shifted in time by an amount $t_{offset}$ = 75 ps. The offset time corresponds to the time it takes the sound to travel through the cavity films once and the thick aluminum and cap silicon dioxide films twice. Using the model discussed in chapter 4, the time $t_{offset}$ should be $T_1 + 2T_2$, where $T_1$ is the time it takes sound to travel through the cavity spacer layer, and $T_2$ is the time it takes the sound to travel through the combined thickness of the thick Al film and cap $SiO_2$ film. The resulting curves are shown in Figure 14. The first echo to arrive, denoted by T, is due to sound that has reflected from the tops of the lines and then returned to the cavity. From the arrival time $t$ of the first echo, the thickness of the water gap can be estimated as $vt/2$, where $v$ is the sound velocity in water. The thickness of the water gap for the

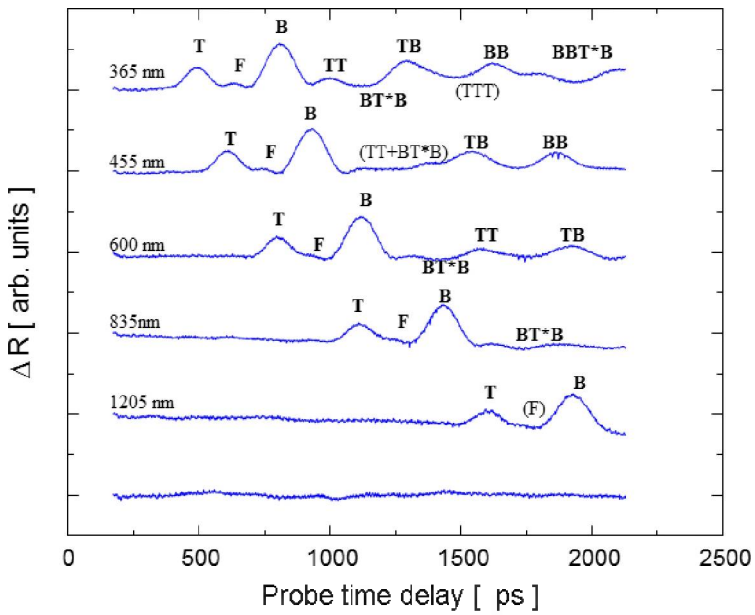


*Figure 14 : POAM data from Figure 6.3 after the background subtraction process. The water film thickness was estimated from the arrival time of the first echo T. Each echo is labeled by a sequence of letters; each T refers to a reflection from the top of the lines and B the bottom of the channel. The feature F always occurred at the same time after T, independent of water film thickness.*

curves in Fig. 6.4 is found to be, from top down, 368, 457, 597, 836, and 1207 nm. The echoes marked B are from sound that has travelled down the channels, reflected off of the bottom, and returned to the cavity. Table VIII lists the arrival times of the first three echoes. The quantity $(B-T)v/2$ was found to match up with the depth of the channels D, provided that the channels were wider than ~100 nm. For channels narrower than 100 nm, the data implied that the velocity of the sound pulse in the channel was up to 10% slower than that in unconfined water.

| T [ ps ] | F [ ps ] | B [ ps ] | $Tv/2$ [ nm ] | $(B-T)v/2$ [ nm ] | $(F-T)v$ [ nm ] |
|---|---|---|---|---|---|
| 493 | 637 | 810 | 368 | 239 | 218 |
| 609 | 753 | 929 | 457 | 241 | 216 |
| 798 | 943 | 1118 | 597 | 240 | 218 |
| 1114 | --- | 1433 | 836 | 240 | --- |
| 1609 | --- | 1924 | 1207 | 236 | --- |

Table VIII: Arrival times of the first three features, *T*, *F*, and *B*, for the data shown in Fig. 14. The quantity $Tv/2$ is the water film thickness and $(B - T)v/2$ the depth of the channels. The quantity $(B - T)v$ was comparable to the pitch of the structure for the curves where the arrival time of *F* was measurable.

There were echoes from sound that has reflected off of the sample and transducer faces multiple times; these are denoted by TT, TB, BB, TTT, etc. There was also an echo visible in many of the curves that occur after the echo B whose arrival time corresponds to an addition round trip through the channel. This echo, denoted BT*B, is from sound that, after reflecting off the bottom, reflected off of the opening of the channel, reflected off the bottom again, and then returned to the cavity. For echoes that have reflected from either the top or the bottom multiple times, there can be multiple contributions that will occur at the same time delay, regardless of the water film thickness. For example, echo BB and TBT*B will always occur at the same time. In addition, there can also be overlap in echoes if the water film thickness has a particular value. An example of this can be seen for the water film thickness of 457 nm in Fig. 14. In this curve, the echoes TT and BT*B arrive at around 1250 ps, and their contributions to the signal overlap. In order to get data where the echo from the bottom was clear, the water film thickness had to be larger than the depth of the channels, otherwise the echo B will be lost among the echoes T, TT, etc. This places a limit on the depth of channel that can be measured, since the deeper the channel is, the larger the water film thickness must be, which in turn will reduce the signal amplitude due to attenuation of the pulse as it travels through the water. One way to avoid this difficulty would be to position the cavity transducer very close to the tops of the lines.

There was a feature in the data at an arrival time which could not be expressed as integer

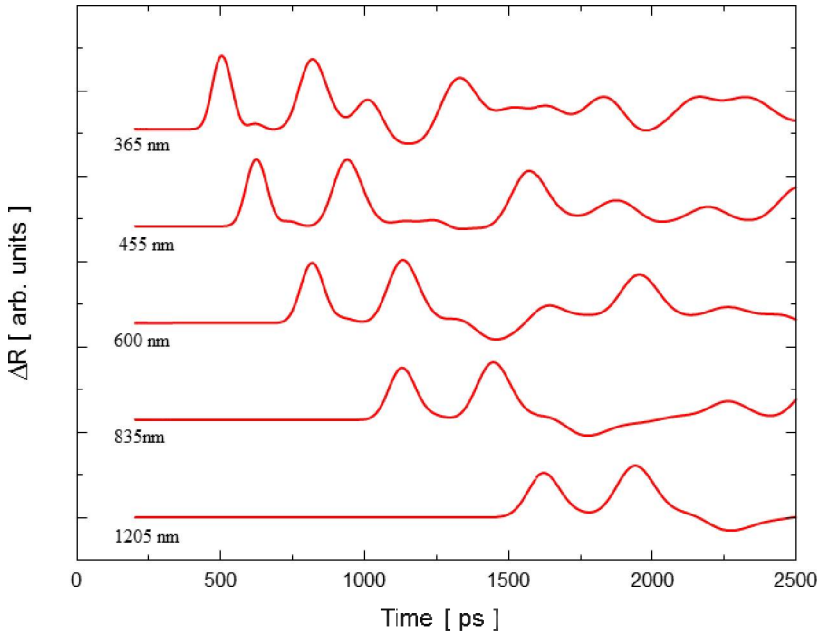


*Figure 15 : Simulated POAM data using the FDTD program discussed in Chapter 5. The dimensions at 5% levels for the structure shown in Fig. 6.2a were rounded to the nearest 5 nm. The mesh size was 5 nm, and the time step was 2 ps. The arrival times agree with the POAM data in Fig. 6.4 qutie well, but there is a discrepancy between the relative sizes of the echoes.*

multiples of the time to traverse the water film thickness and the channel depth. This is denoted by F in Fig. 14. There may possibly be other such features in the data, but overwhelmed by the other echoes. For all of the samples that were studied, the difference in the arrival time of echo T and the peaks in F were independent of the water film thickness. We noticed that the quantity $(F-T)v$ was usually within 15% of the pitch of the structure, but we have not been able to provide a satisfactory explanation for this.

The finite difference time domain (FDTD) program discussed above was used to directly model the signals seen in the POAM experiments. The change in the optical reflectivity of the cavity was assumed to be proportional to the average excess pressure in the fluid at the transducer face. The shapes were modeled as a stack of trapezoids. Depending on the resolution of the simulations, anywhere from 4 to 21 trapezoids were used to model the shape of the structure. Figure 15 shows the simulated POAM data for the structure shown in Fig 12a. The mesh size was 5 nm, and the time step was 2 ps. There is an excellent agreement in the arrival times of the different echoes, but there is a noticeable difference between the relative amplitudes of the various echoes. This will be more fully explored in the next section.

***Sample catalog and outline of results***

Table IX lists the critical dimensions for the samples examined in this work. These are obtained from the SEM measurements.

In the following, the inverse problem of inferring information about the geometry of the sample from the POAM data is explored. Below, the effects of channel width and depth on the amplitude and arrival time are investigated. Further a combination of POAM experimental results and the numerical tools discussed above is used to put an upper limit on the amount of slip that potentially occurs at the water – channel wall boundary.

| Sample | repeat distance P | channel depth D | line width @ 50% L | section |
|---|---|---|---|---|
| A | 360 | 400 | 290 | 6.3 |
| B | 200 | 227 | 135 | 6.3 |
| C | 230 | 410 | 165 | 6.4 |
| D | 230 | 410 | 200 | 6.4 |
| E | 230 | 410 | 180 | 6.5 |

Table IX: Critical dimensions for the structures studied in this work. Dimensions taken from SEM images. All uncertainties are +/- 5 nm.

***Dimensional metrology of periodic nanostructures***

For structures whose POAM data was sufficiently well developed (*i.e.,* the echoes *T*, *F*, and *B* were clearly visible), some information about the critical dimensions *P*, *L*, and *D*, and information about the profile shape could be extracted. For structures where the ratio of channel width to pitch was less than 0.2, the only features that were very prominent were *T*, *B*, and *TT*. The arrival time and amplitude of *B* relative to *T* was found to be quite sensitive to the width and depth of the channel.

***Note on and Comparison with Existing metrology methods***

There are three main techniques for non-destructively measuring nanostructures of this general type. Optical scatterometry[7,8] is a technique based on white light interferometry. While the individual features are unresolvable, the collective effects of a group of structures will alter the signal relative to the signal from an unpatterned area. The average properties of the structures can then be estimated based on a comparison with the results of simulations. CD-SEM[9–13]refers to inferring information about the properties of nanostructures based on top down SEM images with either modeling or a look-up table of the results of previous destructive characterization of the structures being measured. Atomic force microscopy (AFM) techniques [14-20] with special tips have been developed for the accurate measurement of structures with steep side walls. Special techniques to grow sharp tips with metals such as W were developed by Lee[14]. Much work has also gone into exploring the use of reinforced carbon nanotube (CNT) tips. These tips, while capable of high lateral resolution imaging, have their own unique artifacts, such as vibrations of the CNT structure being interpreted as ripples in the profile being measured[19,20].

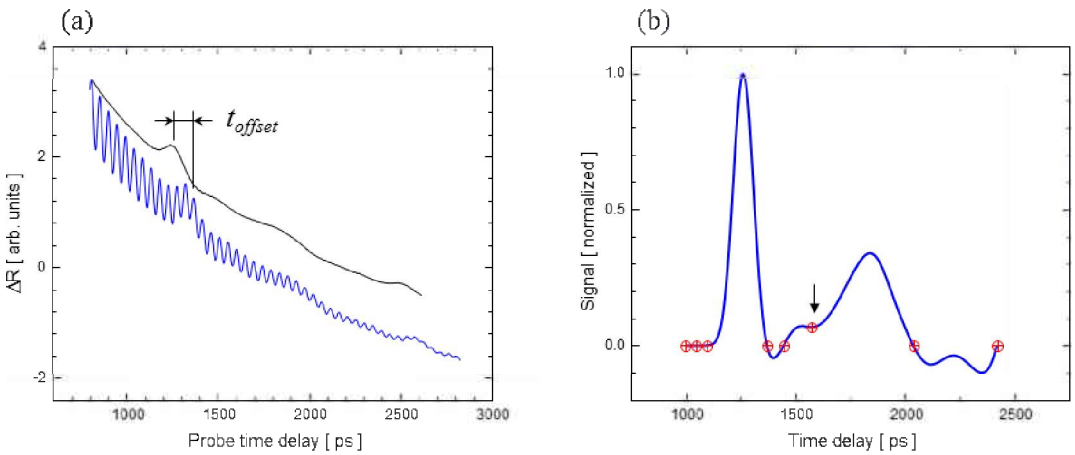


*Figure 16: (a) The experimental data was prepared for the background subtraction process by filtering out the Brillouin oscillations and then shifting the time by $t_{offset}$ = 75 ps. (b) The simulation data to be compared to the experimental data was normalized to the magnitude of the first returning echo. The points in the simulation where the signal is zero were used to generate a piecewise linear background to subtract from the experimental data. If the space between two consecutive zero points was larger than 600 ps, then another point was inserted at a local minima between the two zero points.*

It is noted that CD-SEM and AFM measure individual nanostructures whereas optical scatterometry and POAM measure average properties of an array of structures.

***Procedure for comparing experimental and simulation data***

As an example we consider the POAM data shown in Figure 16a. The lower curve is the signal recorded from the lock-in amplifier, and contains, in addition to the acoustic echoes of interest, a slowly decaying background and fast oscillations. The subtraction of the slowly varying background was necessary for a rigorous comparison of the experimental data to the simulation results. The following procedure was used. First, the Brillouin oscillations were filtered out. The time offset of 75 ps was then applied to give the upper curve in Figure 16a. Then, points in the simulation data where the pressure on the transducer face vanished were found, as shown in Figure 16b. The corresponding points in the experimental data were used as a piecewise linear background function, as shown in Figure 17a. For some simulation results, there were large time gaps between the points where the pressure is zero. In cases where the zero points in the simulation were farther than 600 ps apart, another point was inserted at a local minimum between them; an example is marked by the arrow in Fig. 16b. After the piecewise linear background was subtracted from the experimental data, the experimental and simulation data were both normalized so that the height of the first echo was 1. The offset time for the experimental data was adjusted by 2 ps increments until the best overlap of the first echoes was achieved. Figure 37b shows the results of the background subtraction process for the example experimental data and simulation data sets from Fig 16. Each time an experimental data set was compared to a different simulation result, a different background was subtracted from the experimental data. The goodness of fit of the background subtracted experimental data, $s(t)$, to the normalized simulation data, $n(t)$, was quantified by

$$\chi^2 = \sum_{t=t_1}^{t_2} \left[ s(t) - n_{lin}(t) \right]^2 , \qquad 1.47$$

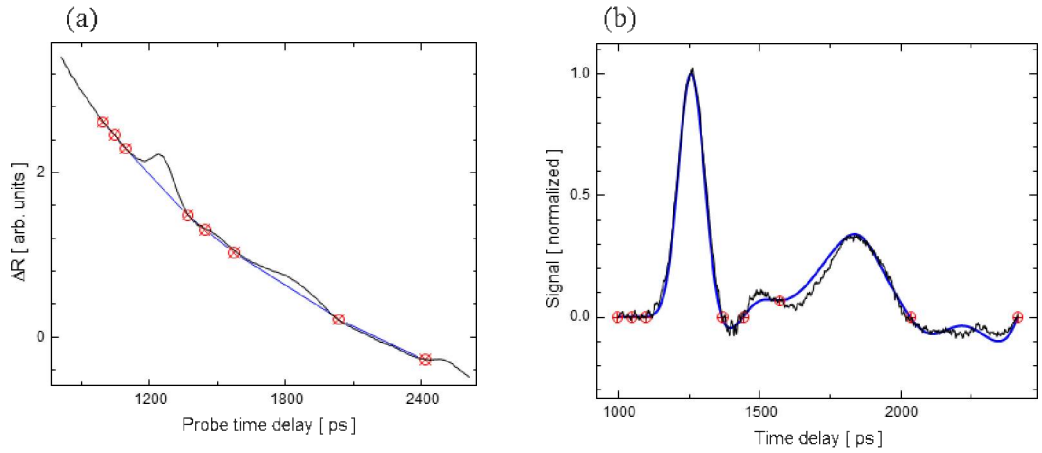


*Figure 17: (a) Typical POAM data, along with the piecewise linear background obtained from the zero points in the simulation data. (b) After the background subtraction, the experimental data was also normalized to the magnitude of the first returning echo.*

where $n_{lin}(t)$ is the linear interpolation of the simulation data at the two time steps that straddle the time $t$, and $(t_1, t_2)$ was the time delay range over which the experimental and simulation data were being compared. The time spacing for the simulations depended on the mesh size. For a mesh size of 5 nm, a 2 ps time step was used, and for a mesh size of 10 nm, 4 ps. The time interval over which the simulations were compared to the experiment was on the order of 1-2 ns.

***Critical dimension and profile metrology of broad channel structures***

A library search method was used to determine the average critical dimensions and profile of the group of structures probed during the POAM measurement. The general procedure was as follows. First, the POAM data were taken on the pattern of interest. The water film thickness was set such that the echo TT did not overlap with either echo B or echo BT*B. A library of simulations was generated for different profiles and critical dimensions $P$, $L$, and $D$. Then each simulation was compared to the experimental POAM data, and the best fit was found.

***• Sample A***

As a first step we made fit to the results of the SEM measurements. Figure 18 illustrates the variety of structure profiles generated for the library used for Sample A. The structures were modeled as a stack of 4 trapezoids. The profile on each side was adjusted at the 0%, 75%, 90%, and 100% height levels in 20 nm increments. The profile codes ran from 0000, which corresponded to a square channel of uniform width, to 3333 which was severely tapered. The profiles were chosen such that the width, from top to bottom, was either constant or increasing, and no overhangs or undercuts were present in this library. For each choice of pitch, line width, and channel depth, eighty different profiles were simulated. Figure 18b shows some examples of the profiles contained in the simulation library generated for sample A.

Figure 19a shows a cross sectional SEM image of sample A. The sample had a pitch of 360 nm, a line width at the 50% level of 290 nm, and a height of 400 nm. The measured width of the channel at 5% height level increments is shown in Figure 19b. The different profiles simulated

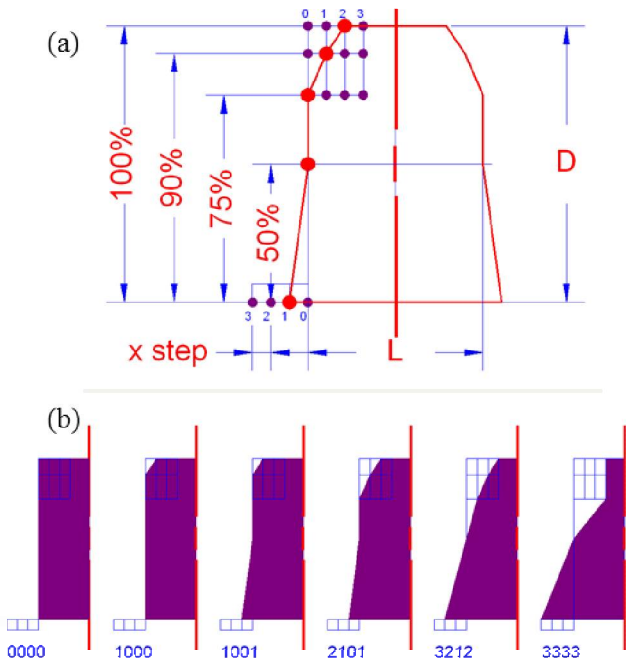


*Figure 18: (a) For each value of P, L, and D, a family of structures with different profiles was generated and their simulations were compared to POAM data for sample A. The width of the line at 4 levels was varied in steps . Each profile had a 4 integer code. (b) Examples of some of the profiles generated. For each value of P, L, and D in the library, there were 80 different profiles simulated.*

for $L$ = 290 nm, $D$ = 400 nm are shown as thin lines. The measured profile falls between profile codes 3110 and 2001, which are denoted by the thicker lines in Fig. 19b.

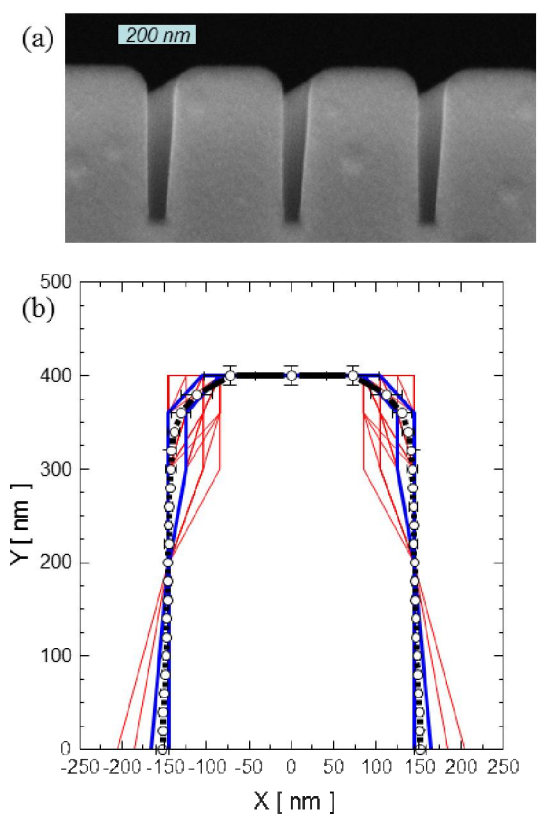


*Figure 19: (a) Cross sectional SEM image of sample A. The pitch of the structure was measured to be 360 ± 5 nm, the channel height 400 ± 5 nm, and the width of the lines at 50% 290 nm. (b) From the SEM cross sectional images, the average profile of over 40 individual lines was measured. The circles connected by the thick line represents the measured average profile of the structure. The thin lines are the 80 profiles generated by the for an L = 290 nm and D = 400 nm. The profile measured by SEM falls in between the two library profiles with codes 3110 and 2001 (denoted by thicker lines).*

We now turn to the construction of a library to compare with the POAM data. In this library, the pitch $P$ was varied from 330 to 390 nm in 10 nm steps, the line width at the 50% level $L$ was varied from 160 to 310 nm in 10 nm increments, and the depth of the channels $D$ was varied from 310 to 460 nm in 10 nm increments. A total of 143,360 simulations were performed.

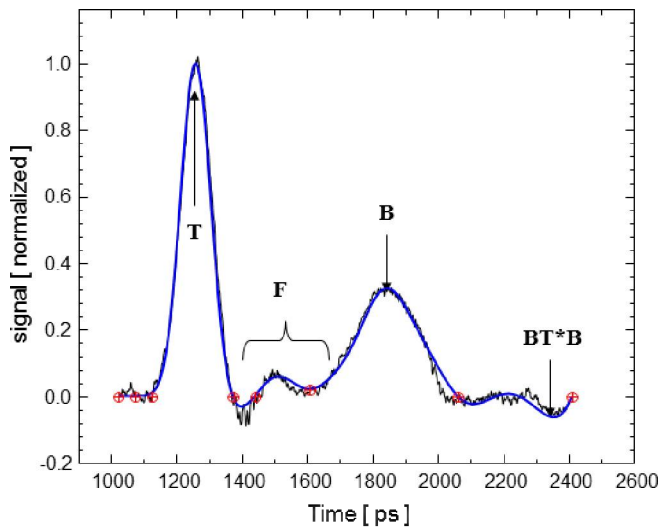


*Figure 20: A comparison of the normalized simulation data for structure (P,L,D) = (360 nm, 270 nm, 400 nm), profile 0001, and the experimental data after background subtraction and normalization.*

First, the search through the library for the best fit was restricted to structures with pitch $P$ = 360 nm, the average value obtained from the SEM measurements. The best fit occurred for $L$ = 270 nm, $D$ = 400 nm, and profile 0001 with $\chi^2_{best} = 0.65$. Figure 20 shows the experimental data and the simulation data for the best fit. The agreement between the simulation and the experimental data for the best fit case was quite good. In Figure 21, the range of line shapes searched is represented by the shaded grey area. The circles with the error bars are the average profile measured from the cross sectional SEM images. The thick line is the profile that had the best fit, and the thinner lines are the profiles from the best 10 fits. Figure 22 is a contour plot of $\chi^2 / \chi^2_{best}$ in the ($L$, $D$) critical space. The best fits are located in the neighborhood of $L$ = 270 – 290 nm and $D$ = 380 – 410 nm.

Figure 23 shows an example of fitting results for (a) $\chi^2 / \chi^2_{best} = 2$, and (b) $\chi^2 / \chi^2_{best} = 5$. For these examples, and almost all of the others that were examined, the echo from the bottom was the most important feature for determining how good the fit was, *i.e.*, how small the $\chi^2$ value was. Figure 24 shows a critical space plot for (a) pitch $P$ = 330 nm, and (b) pitch $P$ = 390 nm. As the pitch was increased, the line widths where the best fits were located also increases. This suggested that the goodness of the fit was mostly determined by the ratio $L/P$.

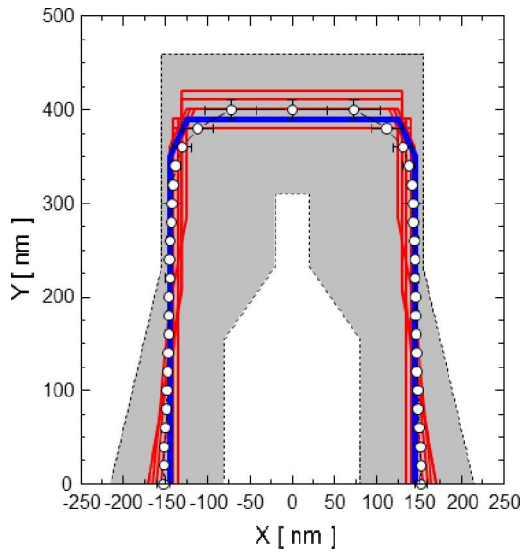


*Figure 21: The shaded grey region represents the range of profiles generated by the library algorithm. The circles are the profile as measured by SEM, while the lines are the profiles of the top 10 best fits. For each value of the pitch, 20,480 structures were simulated and compared to the experimental data.*

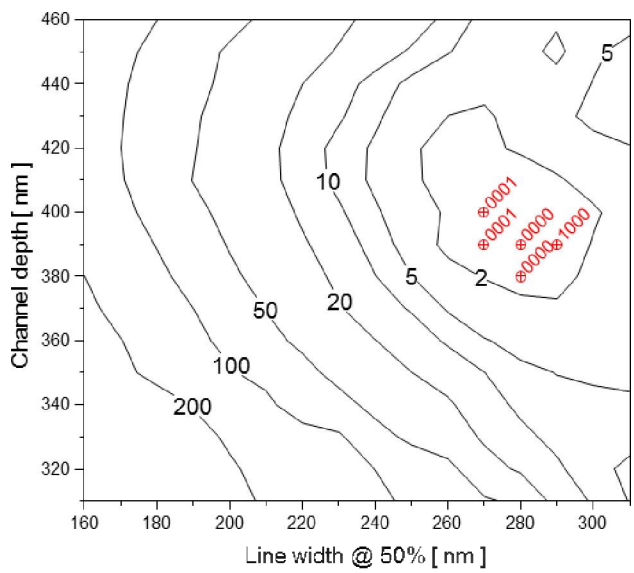


*Figure 22: A contour plot of the best fits in the (L,D) critical space, with P = 360 nm. For each point, there were 80 line profiles simulated and compared to the experimental data. The best value of $\chi^2$ was 0.65 at (L,D) = (270 nm, 400 nm), profile code 0001 (square top, slightly chamfered bottom). The contours mark levels of $\chi^2$ normalized to the $\chi^2$ value for the best fit. The locations of the 5 best fits, along with their profile codes, are marked on the plot.*

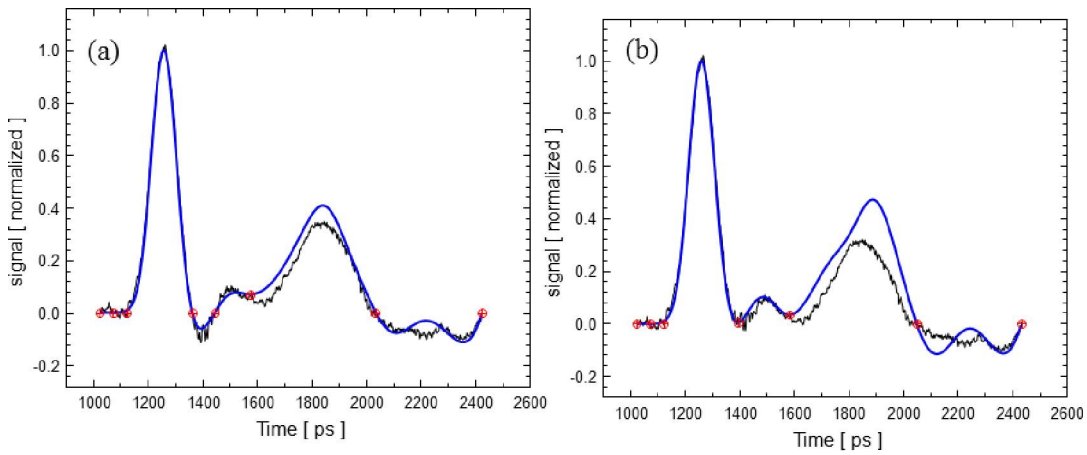


*Figure 23: Typical fits simulated structures with $\chi^2/\chi^2_{(best)}$ values of (a) 2, and (b) 5. The goodness of the fit is dominated by how the echo from the bottom of the channel from the experimental data compares to the simulated data.*

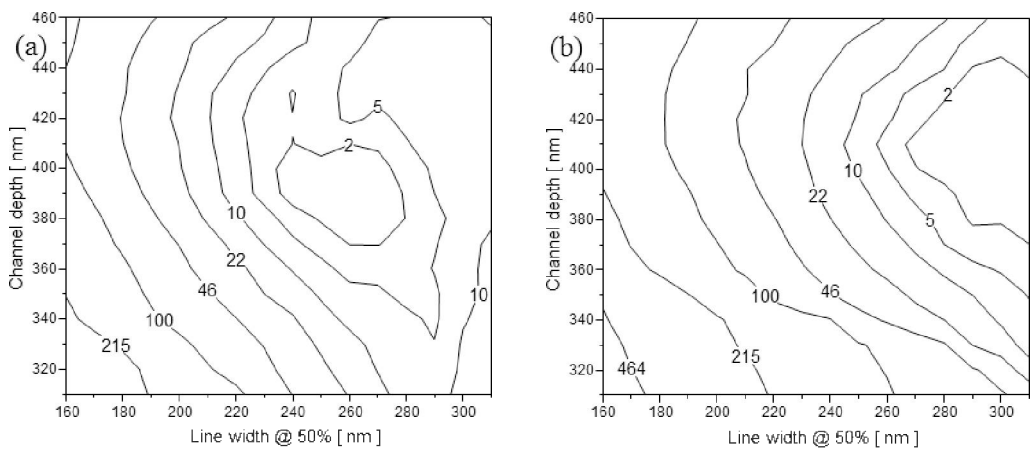


*Figure 24: Contour plots of the critical space (L,D) for a pitch of (a) 330 nm and (b) 390 nm. When the pitch was decreased, the line width where the best fits occurred decreased by corresponding amounts. This suggests that the goodness of the fits were determined not so much by the absolute values of the pitch and line width, but their ratio.*

***• Sample B***

Figure 25a illustrates the method used to generate profiles for the library for sample B. The method was the same as for the library for sample A, except modest overhangs were allowed. The profiles were incremented in 10 nm steps, and the mesh size of the simulations was decreased to 5 nm. Figure 26a shows a cross sectional SEM image of sample B. These lines were measured to be 227 nm tall, with a width at the 50% level of 135 nm, and a pitch of 230 nm. The profiles of 30 different lines were measured from SEM images such as Fig. 26a, and the average of the widths at each height was found. The average line profile is shown by the

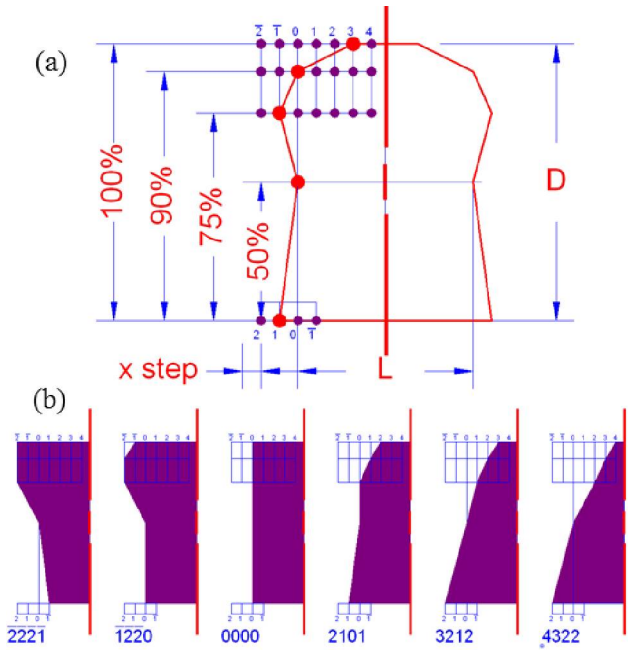


*Figure 25: (a) For each value of P, L, and D, a family of structures was generated. The width of the line at 4 levels was varied in steps . Each profile had a 4 integer code. Examples of some of the profiles generated are shown in (b). For each value of P, L, and D, there were 336 profiles simulated. The profiles in this library were allowed to have undercuts.*

connected circles in Figure 6.16b. For this structure, the SEM profile falls in between profile codes $41\overline{1}1$ and 4300 for $L$ = 135 nm and $D$ = 225 nm, which are shown as thicker lines in Fig. 26b. The 336 profiles that were generated for this combination of $L$ and $D$ are shown as the thin lines in Fig. 26b. A total of 75,264 structures were simulated and compared to the experimental data.

For the library of simulations that was generated for sample B, the pitch was fixed at 230 nm, the line width at the 50% level was varied from 100 to 170 nm in 5 nm increments, and the depth was varied from 180 to 260 nm in 5 nm increments. In Figure 27, the entire range of structures simulated is represented by the shaded grey area, and the average profile measured from the cross sectional SEM image is plotted as open circles. The 10 profiles with the best fit are shown as thin lines. While in the SEM images the profiles show a modest overhang of approximately 10 nm, not one of the top 10 fits shows any overhang. Figure 28 shows the best fit, which occurred for a line width at 50% of 135 nm, channel depth of 225 nm, and profile code 4311.

Figure 29 shows the fitting results for the two profiles from Fig. 26b that bracket the measured SEM profile. For both cases, there is a pronounced disagreement for echoes B and BB. The echoes appear to be quite sensitive to even 10 nm changes in the profile, however, the best fit are not much better than the surrounding ones. Figure 30 is a contour plot of levels of $\chi^2 / \chi^2_{best}$. The best fits are broadly distributed, and there does not appear to be a clear convergence onto the measured values of $L$, $D$, and profile. Some of this may be due to the longer time range over which the experimental and simulation data are compared. The experimental and simulation data

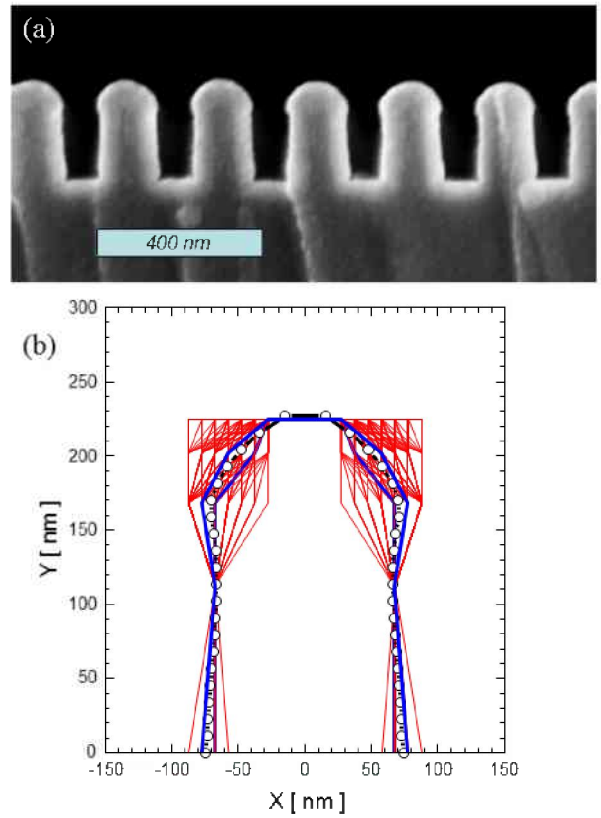


*Figure 26: (a) Cross sectional SEM image of sample B. The pitch of the structure was measured to be 230 +/- 5 nm, the channel height 227 +/- 5 nm, and the width of the line at 50% 135 nm. (b) From the SEM cross sectional images, the average profile of over 60 individual lines was measured. The circles connected by the thick line represents the measured profile of the structure. The thin lines are the profiles generated by the profile algorithm for an L value of 135 nm and D of 225 nm. The measured profile falls in between the two library profiles with codes 4111 and 4300.*

were compared over a larger range of time delays than sample A, and the second set of echoes TT, TB, *etc*. were also included.

### *The effects of channel depth and width on echo B*

For channels that were narrower than 60 nm, the magnitude and arrival time of the echo from the bottom were observed to depend on both the depth and the width of the channel. There was a series of patterns on the samples with decreasing channel widths. Below, results are presented for the narrowest channel for which an echo from the bottom was discernable, and then the next

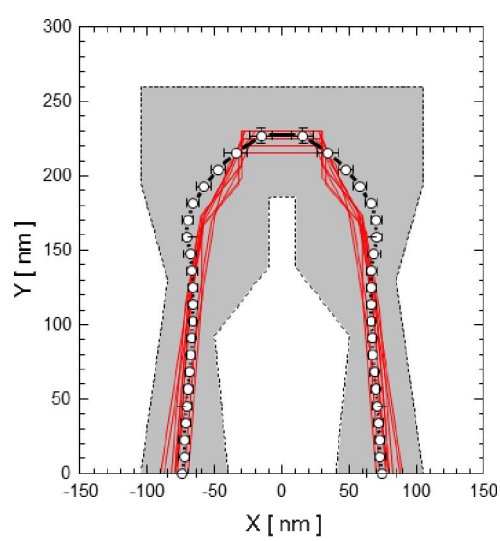


*Figure 27: The shaded grey region represents the range of profiles generated by the library algorithm. The circles are the measured SEM profile, while the lines are the profiles of the top 10 best fits. A total of 75,264 structures were simulated and compared to the experimental data.*

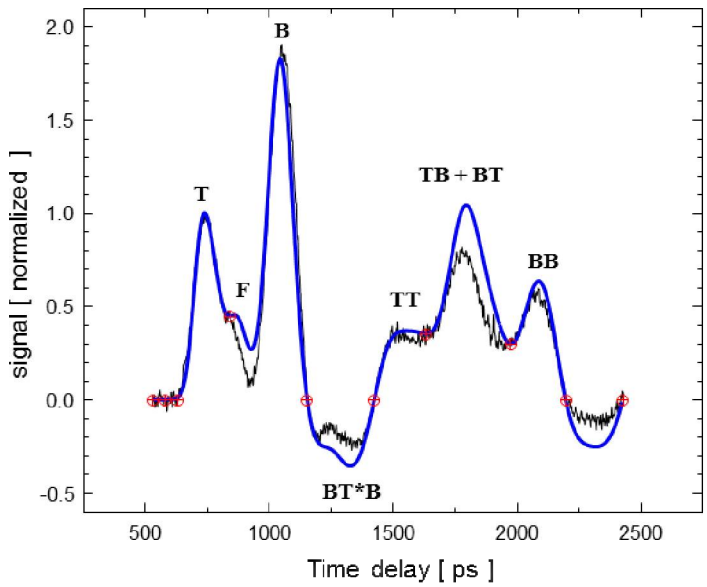


*Figure 28: The best fit found for sample B had (P ,L, D) = (230 nm, 135 nm, 225 nm), profile 4311. Experimental data has had a background subtracted and normalized as described previously. The experimental and simulation data were compared from 530 to 2400 ps, and the best value of $\chi^2$ was 23.75.*

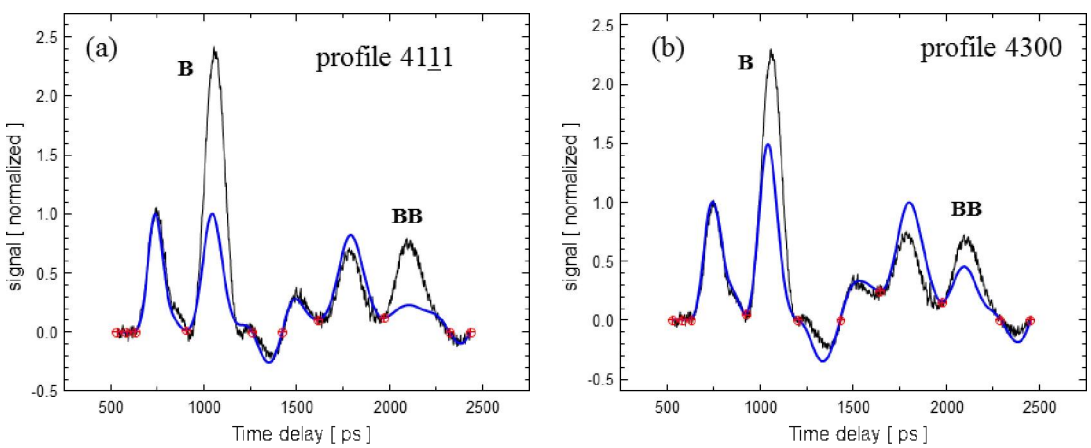


*Figure 29: Results of the background subtraction procedure for the two profiles shown in 6.16b that bracket the profile measured in the SEM. There is a large disagreement between the experimental data and the simulation data for both (a) (P,L,D) = (230 nm, 135 nm, 225 nm), profile 4111, and (a) (P,L,D) = (230 nm, 135 nm, 225 nm), profile 4311. The disagreement is most pronounced for echoes **B** and **BB** in both cases.*

smallest channel, where the echo from the bottom was undetectable. Figure 31a shows a cross sectional SEM of sample C. The white flakes are shards of material from the cleaving process. The profiles of channels 1-6 were measured, and 6 simulations were done (simulation 1 was for an infinite periodic array of channels with profile 1, etc). These are shown in Figure 31b by the curves labeled 1 – 6 (displaced vertically for clarity). It is clear that small variations in the widths caused significant changes in the magnitude of the echo from the

bottom of the channels. The simulations were done with a mesh size of 1 nm and a time step of 0.1 ps. The two experimental data curves shown in Figure 31b were both derived from the same

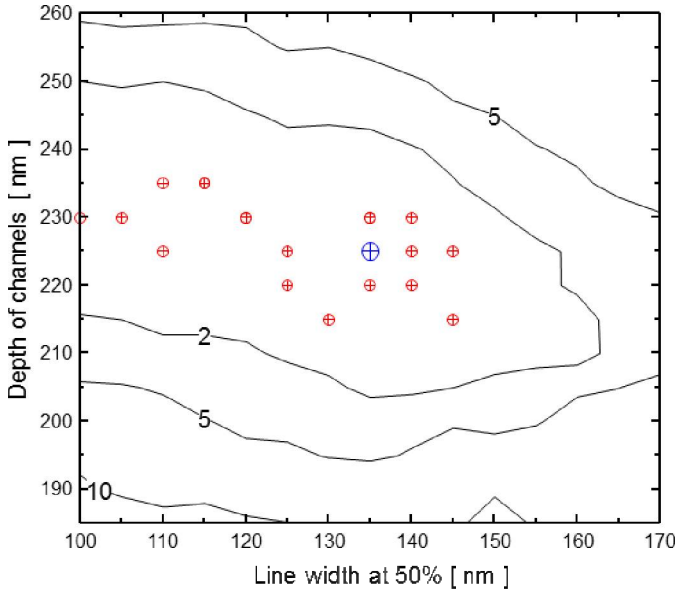


*Figure 30: A contour plot of the best fits in the (L, D) critical space for sample B. For each point (L,D), there were 336 profiles simulated and compared to the experimental data. The best value of $\chi^2$ was 23.75 at (L, D) = (135 nm, 225 nm), profile code 4311. The contours mark levels of $\chi^2$ normalized to the $\chi^2$ value for the best fit. The locations of the 20 best fits are marked by circles on the plot.*

set of data, the only difference between them being how the slowly varying background was subtracted. The lowest simulation curve is for the average profile, with the set of widths as shown in Table X.

*Figure 31: (a) Cross sectional SEM image of sample C. These were the narrowest channels from which an echo from the bottom of the channel could be detected. (b) The profiles of the channels marked 1-6 were measured and simulated, i.e., the scattering of sound from an infinitely periodic array of channels with profile 1 were simulated, and then profile 2, etc. The thick line is the average of the simulations of profiles 1-6, while the two experimental curves are derived from the same experimental data set subjected to two different background subtraction procedures as described in the text.*

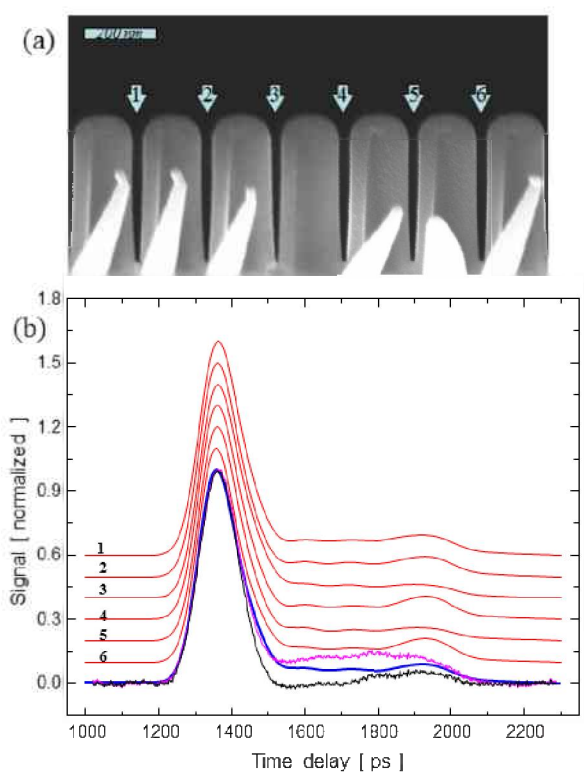

| Height [%] | width [nm] | Height [%] | width [nm] | Height [%] | width [nm] | Height [%] | width [nm] |
|---|---|---|---|---|---|---|---|
| 100 | 134 | 92 | 48 | 75 | 32 | 50 | 32 |
| 98 | 94 | 90 | 40 | 70 | 32 | 25 | 26 |
| 96 | 72 | 85 | 34 | 65 | 32 | 10 | 18 |
| 94 | 58 | 80 | 32 | 60 | 32 | 0 | 12 |

Table X : Channel width versus height level for the average channel of sample C.

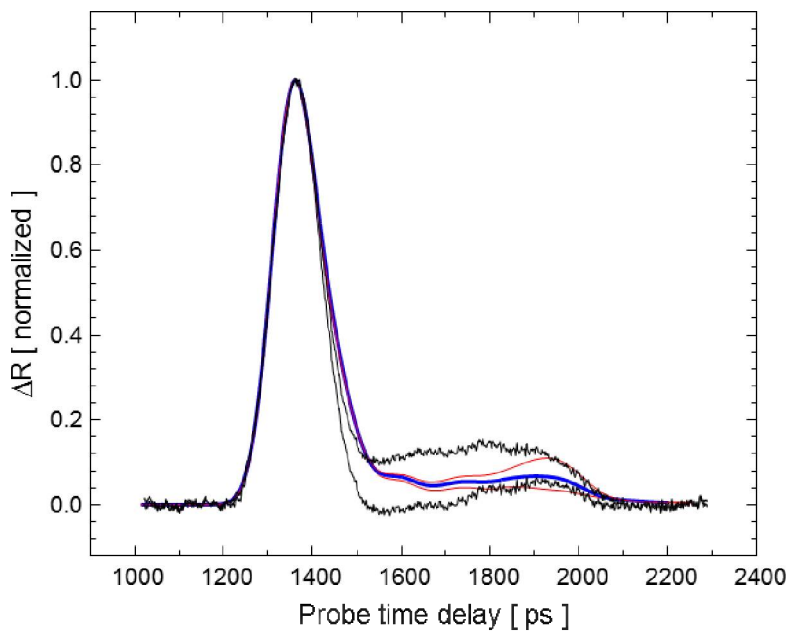


Figure *32*: The thick curve is the simulation result for the average profile of sample C, which had a width of 32 nm halfway down the channel. The lighter curves are for channel widths of 28 and 36 nm. The experimental data shown is the same as that in the previous figure. In this range of channel widths, the magnitude of the echo from the bottom is very sensitive to the channel width.

For sample C, the echo from the bottom was visible, but it was difficult to get an accurate value for the arrival time. This was because the echo was so small that it started to blend in with the structure F that occurred after echo T. The difference in the arrival time of echo T and echo B was measured to be 582 ± 20 ps for the lower experimental curve in Fig. 31b, which would be a round trip through 435 ± 15 nm of water in the bulk. The measured height from the cross sectional SEM was 410 ± 5 nm; in the channel the sound has slowed down and is only traveling at approximately 90 to 95% of the bulk sound velocity. In Figure 32 the experimental data on sample C is plotted alongside simulation results for the average profile. The simulation curve in the center is for the profile in Table X, while for the upper curve all of the widths have been

increased by 4 nm, and for the lower curve all of the widths have been decreased by 4 nm. In going from a channel width of 28 to 36 nm, the amplitude of echo B has more than doubled in magnitude.

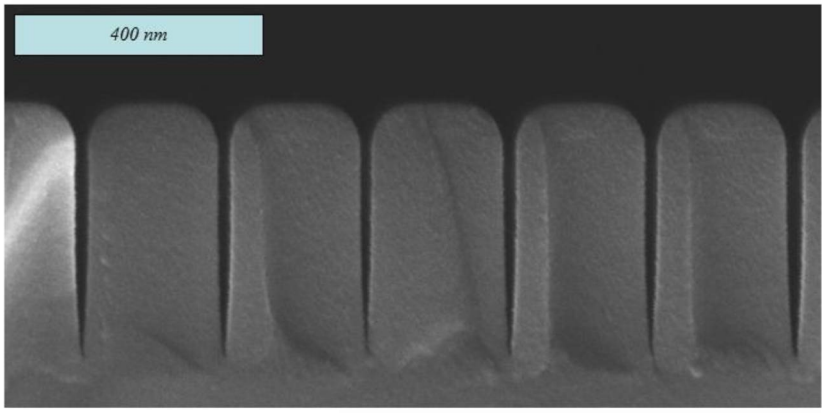


*Figure 33: Cross sectional SEM image of sample D. The width of the channels halfway down was measured to be 24 nm on average, with a range of 20-32 nm.*

Figure 33 shows a cross sectional SEM of sample D. The widths of these channels were the next size down from sample C. These channels were also significantly more tapered at the bottom. For approximately 25% of the channels in sample D whose profiles were measured by SEM, the width at the bottom of the channel appeared to taper right to a point. The average profile measured by cross sectional SEM imaging is shown in Table XI.

| Height [%] | width [nm] | Height [%] | width [nm] | Height [%] | width [nm] | Height [%] | width [nm] |
|---|---|---|---|---|---|---|---|
| 100 | 138 | 92 | 44 | 75 | 24 | 50 | 24 |
| 98 | 98 | 90 | 36 | 70 | 24 | 25 | 18 |
| 96 | 72 | 85 | 24 | 65 | 24 | 10 | 12 |
| 94 | 56 | 80 | 24 | 60 | 24 | 0 | 8 |

Table XI: Channel width versus height level for the average channel of sample D.

Figure 34 shows the POAM data taken on sample D. From the arrival time of echo T, the water film thickness was 755 nm. Moving the sample much closer to the transducer would have resulted in echo TT being superposed on where the echo B was expected to be. The lower simulation data curve is for the average profile from Table XI. The upper curve is for a channel where each of the widths from Table X has been increased by 8 nm.

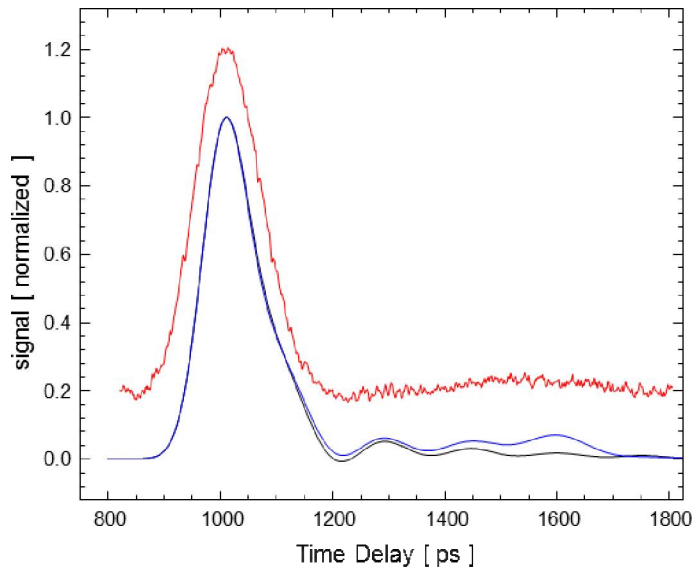


*Figure 34: The top curve is the experimental data taken on sample D (displaced vertically for clarity) after filtering out the Brillouin oscillations and subtracting the background as described previously. Any echo from the bottom is lost in the noise. The lowest curve is the simulation data taken with the average profile measured from the SEM images with a channel width @ 50% of 24 nm. The middle curve shows a simulation for a channel with the same profile as sample C but with a channel width @50% of 32 nm.*

One very important factor that determines the visibility of the echo from the bottom is the ratio of the channel width to the pitch. Samples C and D had channels that were much narrower than the pitch, and most of the sound incident on the structures reflected off of the top. It is possible that for arrays of narrow channels with smaller pitches, the echo from the bottom will be more visible.

***Estimating slip length with POAM measurements***

In this section, the experimental data and the combined results of the time and frequency domain simulations are used to place an upper limit on the possible slip length at a water/silicon nitride interface. The simulation results presented below suggest that for channels with width less than 100 nm, the presence of slip will have a significant effect on the arrival time and magnitude of the echo from the bottoms of the channels. While it is difficult to measure the absolute magnitude of the echo from the bottom due to uncertainties introduced by the background subtraction process, it was possible to measure the round trip time in the channel with an uncertainty better than 10 ps. In what follows, this uncertainty in transit time is translated into an estimate on the slip length at the side walls.

***POAM and the estimation of slip length***

In the POAM estimates of slip, the time it takes the sound pulse to travel in the channel is compared to the results of the FDTD simulations. The solid in the FDTD simulations was modeled as a liquid whose properties were the same as water, except the density was taken to be a factor of $10^6$ times larger than that of the water. This resulted in essentially no slip at the interface. The difference in the arrival times of echoes T and B was measured and compared to the results of the FDTD simulation, and the difference between simulation and experiment was

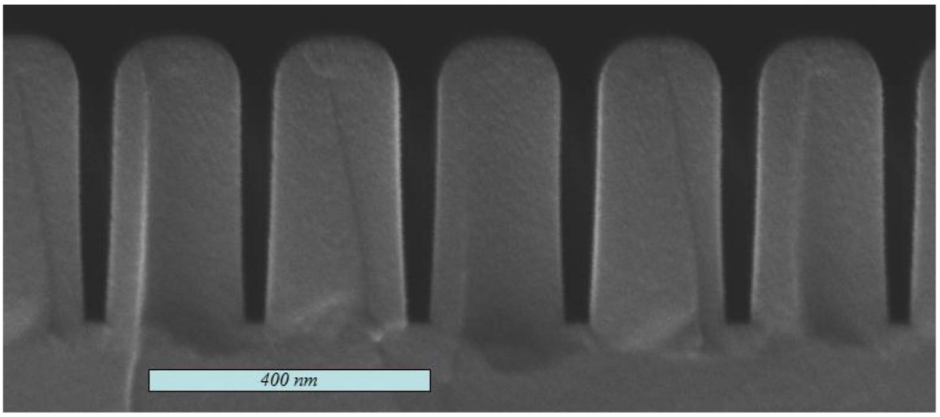


*Figure 35: Cross sectional SEM image of sample E. The width of the channels halfway down was measured to be 52 nm on average, with a range of 48 – 54 nm.*

translated into a slip length with the aid of the frequency domain numerical results discussed above.

### *Choice of sample*

Figure 35 shows a SEM cross sectional image of sample E. This structure was chosen for the slip experiments from consideration of two factors. For a fixed slip length, the effect of slip will be more pronounced for narrower channels than wider ones. However, of the channels that were available the profile became more tapered as the width decreased. For example, in Fig. 33 the average width of the channel at the 50% level was 31 nm, but at the bottom the average width of the channel was 11 nm. For the wider channels, such as those in sample A, the width from the 85% level to the bottom only varied by at most 10 nm, but for these broad channels the effects of a slip length of 2 – 5 nm will become less pronounced. The dimensions and profile of sample E represented a compromise between narrowness and uniformity among the available patterns.

Several SEM images like that in Fig. 35 were taken and the profiles of 20 channels were measured, and then the width at each height level was averaged to determine the profile of the "average" channel. This was the profile that was then used in the time domain simulations. The average widths of the channels as a function of height are listed in Table XII.

| Height [%] | width [nm] | Height [%] | width [nm] | Height [%] | width [nm] | Height [%] | width [nm] |
|---|---|---|---|---|---|---|---|
| 100 | 168 | 92 | 70 | 75 | 56 | 50 | 54 |
| 98 | 120 | 90 | 62 | 70 | 56 | 25 | 48 |
| 96 | 96 | 85 | 56 | 65 | 56 | 10 | 42 |
| 94 | 80 | 80 | 56 | 60 | 56 | 0 | 36 |

Table XII: Channel width versus height level for the average channel of sample E.

The uncertainty in the average widths was estimated by

$$\sigma = \sqrt{s^2 + 2l^2} \quad 1.48$$

where $s$ is the standard deviation in the widths of the channels that were measured, and $l$ is uncertainty in the location of the edge in the cross sectional SEM image. For the image shown in Fig. 35, $s$ was around 3 nm and $l \sim 4$ nm, giving an uncertainty in the widths of about 6 nm.

***POAM data and FDTD simulations***

Figure 36a compares the experimental data and the time domain simulation data, and Figure 36b

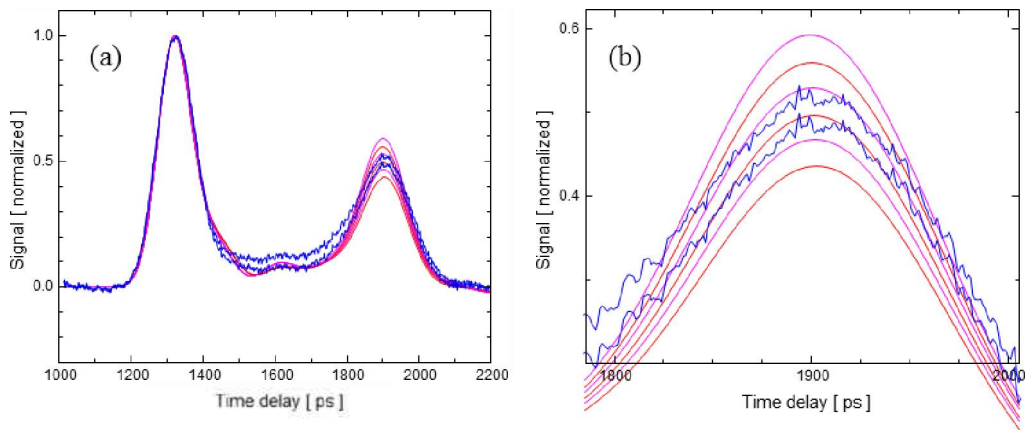


*Figure 36: Simulation vs. experiment for sample E. The two curves with noise are the same experimental data with the background subtracted two different ways (see description for sample C). Also plotted are a series of simulations with increasing channel width, starting at 60 nm and increasing to 70 nm in 2 nm increments. (b) Close up view of the echo from the bottom from (a). The arrival time of the echo from the bottom appears to be consistent with the no slip condition enforced by the simulation program.*

shows a close up of the echo from the bottom of the channel. From bottom to top, the simulation results are for channels with a width at the 50% level of 60, 62, 64, 66, 68, and 70 nm. The amplitude of the echo B for the experimental data agrees with the simulation results for a channel width between 62 and 68 nm, but the measured width was almost 10 nm less than this. The origin for the discrepancy between the simulation and experimental results was attributed to the difficulties associated with the background subtraction. The travel time in the channels for the experimental data and the simulation results were the same to within ±12 ps, and the round trip time could be measured with an accuracy of 2%. The experimental result for the arrival time of echo B was more robust to the background subtraction process as well.

***Frequency domain simulations for slip and no slip cases***

Using our developed numerical method, the phase velocity as a function of frequency for several combinations of channel width and slip length was computed. The resulting curves are shown in Figure 37. The phase velocity has been normalized to the value of the sound velocity in water. The three lowest curves are for channels 48, 60, and 70 nm wide, respectively, with a no slip boundary condition. The dependence of the phase velocity on the channel width is demonstrated; sound travels faster down wider channels for all frequencies. The curves labeled 4, 5, and 6 are

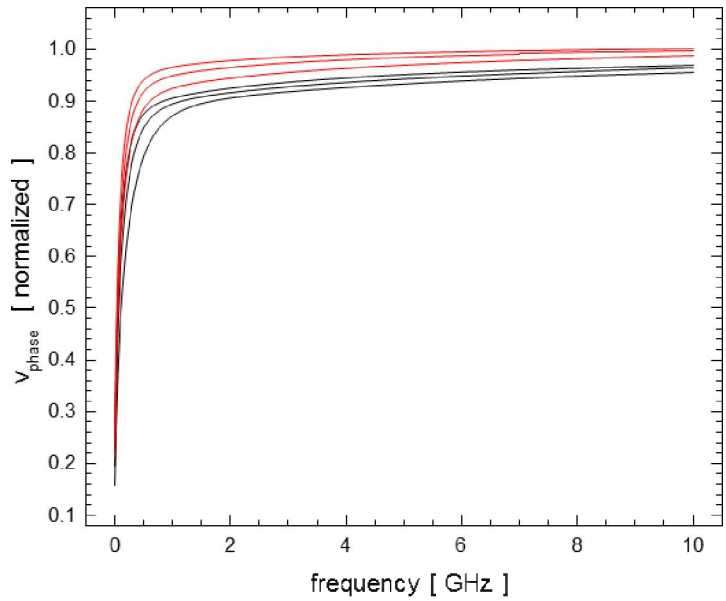


*Figure 37: Relative phase velocity (normalized to the bulk sound velocity) versus frequency for several values of channel width and slip length. The three lower curves, starting at the lowest, have widths of 48, 60, and 70 nm, and no slip. The three upper curves all have a channel width of 60 nm, and slip lengths of 2, 5, and 8*

the results for a channel that is 60 nm wide with a slip length of 2, 5, and 8 nm at each boundary. The presence of slip at the boundary significantly increases the phase velocity. Figure 38 shows the amplitude attenuation as a function of frequency. The presence of slip significantly decreased the amplitude attenuation for waves propagating along the channel.

Let $v_{phase}(f,w,b)$ be the computed phase velocity as a function of frequency $f$ for a channel width $w$ and slip length $b$. In Figure 5.29, the expression

$$\frac{v_{phase}(f,w,b)-v_{phase}(f,w=60\text{ nm},b=0\text{ nm})}{v_{phase}(f,60\text{ nm},0\text{ nm})}\times 100 \qquad 1.49$$

is plotted versus frequency for each of the curves in Fig. 38. The upper and lower bounds of the shaded grey area are for channel widths of 48 and 70 nm with no slip, respectively. The shaded area represents possible variations in the phase velocity due to variations in the channel width from channel to channel. The solid curves are all for channels with a width of 60 nm and increasing amounts of slip (2, 5, and 8 nm). From the above results, the slip length at the side wall water interface was estimated to be less than 5 nm.

***Comments on extending the technique to other fluid/solid interfaces***

The above results deal with possible slip at the interface between the walls of the channels and water. In order to make a measurement, a sample with channels like that shown needs to be fabricated. This is the main disadvantage of using a POAM measurement to investigate the slip at interfaces, since slip measurements are usually done on surfaces that are treated in certain ways, either chemically or physically. If the sound was focused into the mouth of one channel

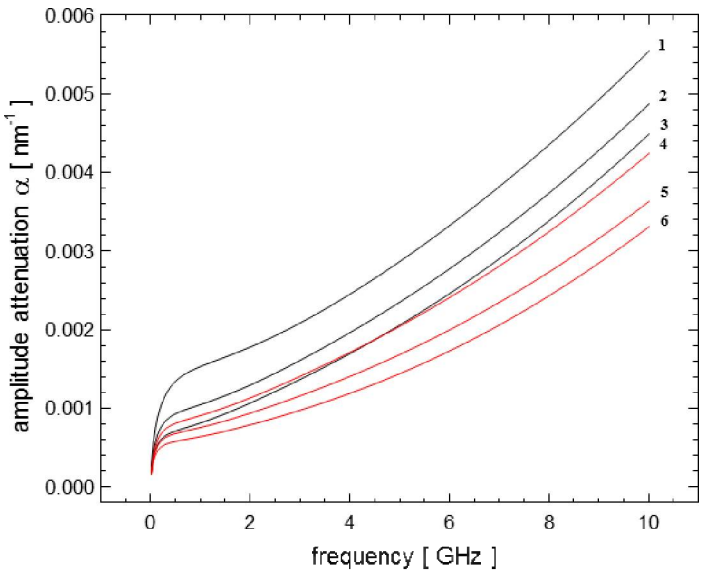


*Figure 38: Amplitude attenuation versus frequency for several values of channel width and slip length. Curves 1-3 are for the no slip case and have widths of 48, 60, and 70 nm. Curves 4-6 are for channels with a width of 60 nm and slip lengths of 2, 5, and 8 nm.*

with an acoustic lens, *i.e.*, if a similar measurement was performed using a scanning opto-acoustic microscopy (SOAM) technique, then the sample preparation and characterization would be less cumbersome, since only 1 channel would need to be prepared instead of an array of them.

***Summary Comment on POAM Data and Capabilities***

Results of POAM measurements of 1D periodic nanostructures were presented. The relative sizes of the echoes in the POAM data were used to infer information about the average critical dimensions and profile of groups of structures. For structures with channels that were less than 60 nm wide, the amplitude and arrival time of the echo from the bottom of the channels were very sensitive to the channel width and depth. POAM was shown to provide a way of measuring the dimensions of these features nondestructively. For narrow channels, the presence of slip between the water-side wall interface would have a measurable effect on the echo from the bottoms of the channels. POAM data was used to place an upper limit of 5 nm on the slip length at the water-silicon nitride interfaces.

**<u>II.B. Phase II</u>: Design, Fabrication, and Demonstration of a Focusing Acousto-Optic Microscope (SOAM)**

The idea of scanning acoustic microscopy dates back to 1937 when Sokolov applied for a patent for a device to detect the flaws within materials by acoustic waves. The US patent was issued in 1939[21] but the application was restricted to the description of a possible design for such a microscope. Since then much progress has been made towards a useful acoustic imaging microscope. In 1959 Dunn and Fry[22] reported on experiments with a simple microscope operating in transmission mode. A plane sound wave of frequency 12 MHz was incident on the sample and spatial variations in the transmitted intensity were measured using a thermocouple probe as a detector. Significant further progress was made by Lemons and Quate[23] who constructed a scanning transmission microscope using focused ultrasound (rather than planar) at 160 MHz, together with an acoustic lens to collect the sound. Further work by this group extended the frequency range up to 4.4 GHz and achieved a resolution of 200 nm.[24]

Schematic generic diagrams of transmission and reflection acoustic microscopes are shown in Fig. 39. Currently, the reflection microscope is of most interest. This geometry

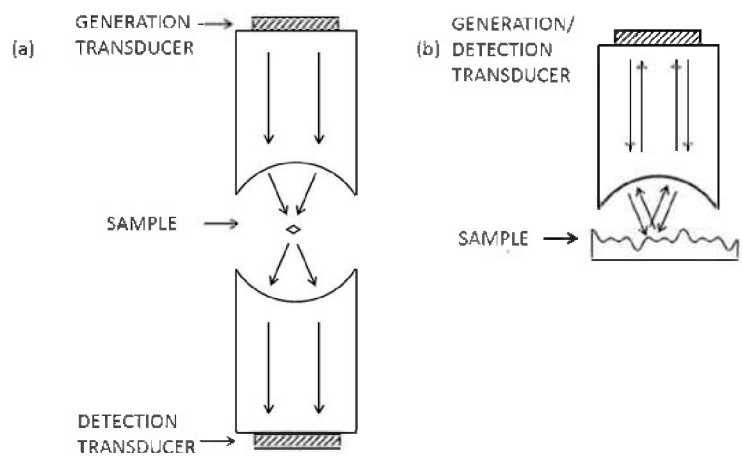


***Figure 39. Schematic diagram of (a) transmission and (b) reflection acoustic microscopes.***

gives information about surface topography from the reflection of the sound at the interface between the liquid coupling medium (CM) and the sample. The sound will also penetrate into the sample and consequently elastic properties of the material near to the sample surface can be studied.

The resolution $d$ of an acoustic microscope is related to the sound wavelength $\lambda$ by

the formula

$$d = \frac{0.51\lambda}{NA}, \tag{1}$$

where $NA$ is the numerical aperture. However, the attenuation of sound in most liquids, (water is the CM normally used), increases as the square of the frequency. As a result, for a given path length between the lens and the sample, there is a maximum frequency which can be used, and a minimum wavelength which limits the spatial resolution. To reduce the wavelength and to improve the resolution it is therefore necessary to decrease the travel distance through the CM. In water, the attenuation coefficient $\alpha$ per unit distance is $\beta f^2$ where $f$ is the frequency and $\beta = 19 \times 10^{-17}$ sec$^2$ cm$^{-1}$ at 30 C.[25] Therefore, the amplitude of a 10 GHz sound wave is reduced by a factor of $\exp(-1.9) \simeq 0.15$ after traveling 1 μm. Because the attenuation is proportional to frequency squared, the attenuation of the high frequency components results in a pulse profile which is a Gaussian with full width at half maximum of $\frac{2\sqrt{\ln 2}}{\pi} v\sqrt{\beta L}$ where $v$ is the sound velocity and $L$ is the distance traveled. When $L = 1$ μm, this width is 0.11 μm, and for 0.3 μm it is 60 nm.

Decreasing the travel distance requires the use of a very short sound pulse. This is because there is always substantial reflection of sound at the interface between the focusing/collecting acoustic lens and the CM. Thus, in the reflection acoustic microscope, for example, the signal of interest comes from the sound which has been transmitted into the CM, reflected at the surface of the sample, and then passed across the interface back into the lens. There will also be an unwanted signal of comparable magnitude which has been reflected at the CM to lens interface and then bounced off the sample a second time. To separate these in time, the total length of the sound pulse when it is in the CM has to be significantly less than the diameter of the lens. With conventional ultrasonic techniques using electrically-driven piezoelectric transducers, it is very difficult to generate sound pulses shorter than a few nanoseconds, and this limits the smallest possible travel distance. However, it is possible to use light pulses to generate and detect much shorter sound pulses,[26] and for this reason we have used this technique in conjunction with specially designed and monolithically integrated optoacoustic focusing transceivers. To fully employ this technique for a practical acoustic microscope requires the solution of a number of experimental problems and this is the focus of the present paper.

In the picosecond ultrasonic technique a short light pulse is absorbed in a metal or semiconductor sample thereby setting up a thermal stress near the surface. The stress relaxes and a strain pulse is generated which propagates into the sample. When the strain

pulse reaches an interface it is partially reflected, and the reflected component returns to the surface. This results in a change in the optical reflectivity of the surface which is measured with a time-delayed probe light pulse. The technique makes possible ultrasonic experiments on thin films, and attenuation measurements have been made at frequencies up to several hundred GHz.[27]

***Scanning Optoacoustic Microscope (SOAM) design***

The design of the microscope is shown schematically in Fig. 40. The structure for generating and detecting sound is fabricated on the lower surface of a 500 μm glass wafer. An optical cavity is formed by a 230 nm $SiO_2$ film which is sandwiched between a 7 nm Al film deposited on the substrate and a lower 50 nm Al film. The acoustic lens is fabricated within a 1.8 μm Al or $SiO_2$ film deposited below the optical cavity by a method we describe below.

The optical cavity is necessary to improve the signal-to-noise ratio in the experiment. The changes in optical reflectivity in the all-optical picosecond ultrasonics experiments to

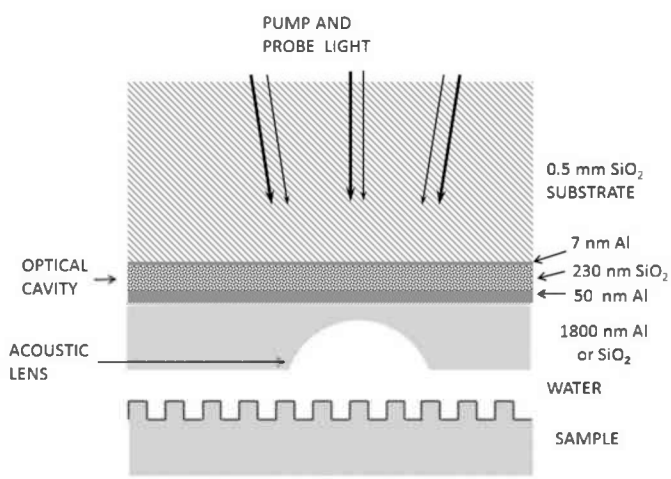


***Figure 40. Schematic diagram of the scanning opto-acoustic microscope***

study sound propagation in solids are small, typically of the order of $10^{-5}$, but can be measured without much difficulty. However, in an acoustic microscope the signal is reduced because of the partial transmission of sound across interfaces and because of the attenuation. A sound pulse going from medium 1 to medium 2 and then returning to medium 1 is reduced in amplitude by the factor $4Z_1Z_2/(Z_1+Z_2)^2$, where $Z_1$ and $Z_2$ are the acoustic impedances. For aluminum and water $Z_1/Z_2 = 11.7$ and so the amplitude is reduced by a factor 0.29. The use of an optical cavity has been described in earlier papers by our group[28,29]. The optical cavity increases the absorption of the

generating pump light pulse (relative to the absorption which would occur for a single Al film), thereby increasing the amplitude of the generated sound. When the sound pulse returns after propagating through the water and being reflected at the sample, it results in a change in the cavity spacing and an enhanced change in reflectivity of the probe light. As discussed previously,[28,2Error! Bookmark not defined.] the optimization of the design for the cavity has to take into account several factors:

1) As far as the choice of materials is concerned, it is advantageous to choose all materials in the cavity structure with nearly the same acoustic impedance. This is to minimize reflection of sound at the interfaces. The amplitude reflection coefficient at a $SiO_2$/Al interface is ~10%.

2) In order to maximize the absorption of the pump it would be best to make the width of the cavity such as to give a minimum reflectivity. However, if the width were chosen this way there would be no change in the reflectivity of the probe light (assuming this had the same wavelength as the pump) when the sound changed the cavity spacing.

3) A high Q factor of the cavity increases the change in reflectivity due to a change in spacing. However, in order to focus the pump and probe beams onto the area above the acoustic lens it is necessary to use a high numerical aperture lens. Thus, these beams are composed of light with a range of propagation directions and each direction needs a slightly different cavity spacing to be in resonance. Thus, there is a limit to the highest Q that can be used.

In the current experiment we have used a 60x objective with focal length 1 cm to focus both the pump and probe beams. The diameters of the beams incident on the lens were approximately 3 mm. This setup made it possible to focus onto a spot on the acousto-optic cavity of about 3 μm diameter. The laser source had wavelength 800 nm, with pulse width of 200 fs and 80 MHz repetition rate. The spectral width of the laser output is approximately 12 nm. We used two laser line filters to set the pump and probe beams at slightly different wavelengths; 809 nm for the pump and 806 nm for the probe. This made it possible to have the probe at a wavelength where the reflectivity of the cavity changed most rapidly with spacing, while the pump had a wavelength at which the absorption of energy was higher. The pump and probe beams had powers of 7 mW and 4 mW, respectively, and the pulse energy applied per unit area was about 1 and 0.5 mJ $cm^{-2}$, respectively.

The remainder of the experimental setup follows the standard pump-probe measurement technique for ultrasonics.[2Error! Bookmark not defined.] The pump beam was modulated by an electro-optic modulator at 1 MHz, and the output of the detector of the reflected probe light was fed to a lock-in amplifier using the 1 MHz as reference. A third laser line filter passing 806 nm was put in front of the probe photo-detector to reduce the effects of scattered pump light.

To scan the lens across the sample we used the translation stage shown in Fig. 41. In the figure, part A is a square "A" shaped frame bolted onto the bottom plate E. On the top center of A, there is a holder for the structure comprised of the optical cavity and acoustic lens; this has an opening for access of the pump and probe laser beams coming from above. The sample to be tested is mounted on the sample holder B with its surface aligned approximately parallel to the bottom of the optical cavity/acoustic lens structure. The sample holder is bolted onto a P-517.3CL nano-positioning stage C from Physik Instrumente.[30] This has a 100 μm moving range in the $x$ and $y$ directions and 20 μm in the $z$ direction. In addition, a coarse adjustment of the sample height with moving range of about 1 mm and 0.02 radians in the tip-tilt angle was provided by a Kelvin clamp between the plate D and the base plate E.

### *Design and Fabrication of the Integrated Acoustic Lens*

For this experiment we needed to have a concave acoustic lens and wanted to make the numerical aperture as large as possible. Consider first the design of an aluminum lens.

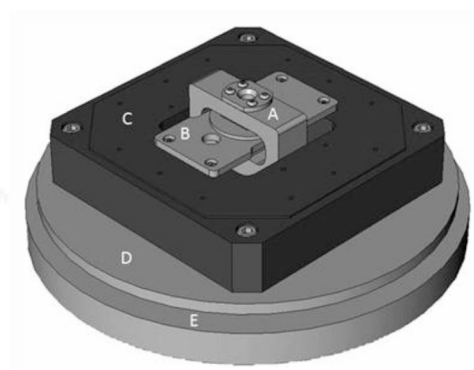


***Figure 41. Translation stage. The functions of the different components are described in the text.***

The construction of the lens is made easier because of the large difference between the sound velocity $v_1$ in aluminum ($6.42\times10^5$ cm s$^{-1}$) and the velocity $v_2$ in water ($1.49\times10^5$ cm s$^{-1}$ at 23 C). This difference reduces the effects of spherical aberration. Let the axis of the lens coincide with the $z$-axis, and the location of the lens surface be $z=\zeta(r)$ where $r$ is the distance from the $z$-axis, with $\zeta(0)=0$. In the experiment an essentially planar sound pulse propagates in the positive $z$-direction. Based on geometrical optics (actually geometrical acoustics), one can show that in order for all of the incident sound to come to a focus at the on-axis location $r=0,\ z=f$, the lens has to be aspherical with profile

$$\zeta(r) = \frac{v_1}{v_1 + v_2}\left[ f - \sqrt{f^2 - \frac{v_1 + v_2}{v_1 - v_2} r^2} \right]. \tag{2}$$

For small values of $r$

$$\zeta(r) = \frac{v_1}{2(v_1 - v_2)} \frac{r^2}{f}. \tag{3}$$

Thus the radius of curvature of the region of the lens near to the axis is

$$R = \frac{v_1 - v_2}{v_1} f \tag{4}$$

As an example, we show in Fig. 42 the calculated profile for an aspheric lens with $f = 2$ μm, along with the profile of a spherical lens of radius given by Eq. 4, i.e., $R = 1.537$ μm. One can see that the difference between these two lens profiles is very small. In addition, the transmission of sound from aluminum to water decreases rapidly as the angle of incidence to the lens surface increases making the contribution to the signal at the focus from the outer part of the lens unimportant. For these reasons we have not tried to make lenses with non-spherical profiles.

A wide range of techniques has been used for the fabrication of microlenses for optical applications.[31] Convex lenses can readily be made by deposition of a thin film, patterning

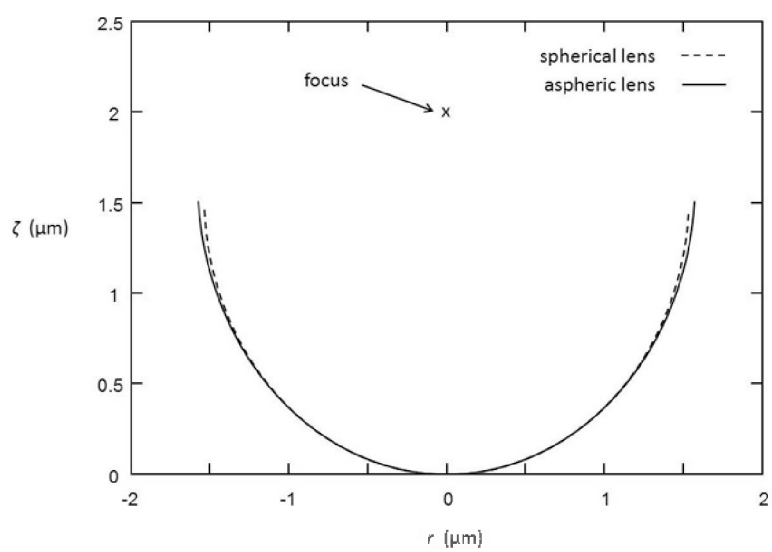


***Figure 42. Comparison between the shape of an aspheric lens and a spherical lens.***

into dots, and followed by reflow.[32] Concave lenses have been made by first depositing a thin metal film onto a substrate, making a small hole in the film, and then wet etching the substrate through the hole.[33] We attempted to make lenses directly on a $SiO_2$ substrate using this method but the lenses did not have an acceptable (ideal) profile.

We therefore developed a process for lens fabrication based on nanoindentation of aluminum. The simplest approach would be to press the nanoindenter tip directly into a metal film. However this would require an indenter tip with a shape which was accurately spherical. Instead of using a tip like this, we used a tip with an almost flat end face to press a silica sphere into an aluminum film. We first deposited an approximately 2 µm aluminum film using electron beam evaporation. This film was then patterned into round

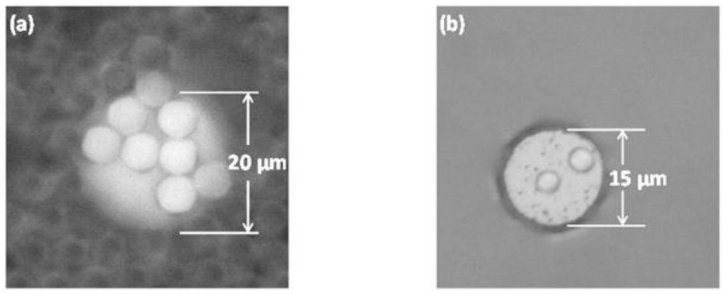


***Figure 43. (a) Optical image of 5 µm silica spheres on a 20 µm diameter aluminum island. (b) Optical image of two acoustic lenses formed after indentation and removal of silica spheres on a 15 µm diameter island***

islands with diameters of 10, 15, 20, 25 or 30 µm by photolithography. Having different size islands made it easier to locate a particular island after nanoindentation. A drop of water containing about $10^7$ silica spheres per $cm^3$ was then put on the film, and the water was then allowed to slowly evaporate. This left a single layer of spheres attached to the islands by the van der Waals force, as shown in Fig. 43a. After indentation using a Hysitron nanoindentor with diamond tip TI-046,[34] we removed the spheres by sonicating the sample in water. We have made lenses with radius of curvature between 0.5 and 2.5 µm in this way, and can control the numerical aperture through the choice of the depth that the sphere goes into the film. This method has the advantage that the indentation reduces the roughness of the surface of the film. An example of lenses made in this way is shown in Fig. 43b. The result of an AFM measurement of the profile of a lens made using a 2.5 µm sphere is shown in Fig. 44.

The nanoindentation method can only be used with ductile materials. To make lenses in

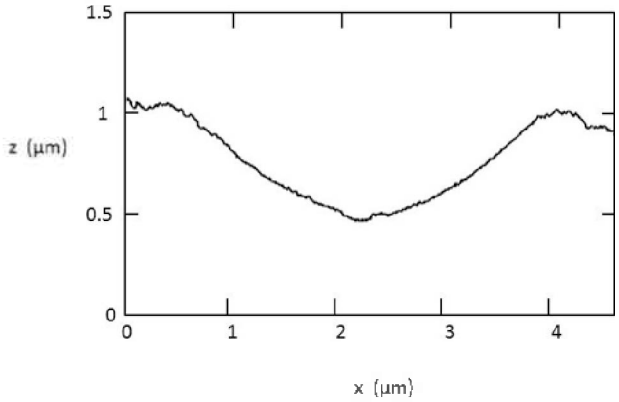


***Figure 44. Profile of a lens made using a 2.5 µm silica sphere. The x-axis is along a line passing through the center of the lens.***

silicon dioxide we have used a focused ion beam (FIB).[35] We first prepared the Al and $SiO_2$ films for the optical cavity. We then sputtered onto the outer Al film a 700 nm layer of $SiO_2$. A thin layer (5 nm thickness) of Cr was next deposited by e-beam evaporation onto this $SiO_2$ film. We then deposited some small platinum target patterns onto the Cr using Ga-ion beam assisted chemical vapor deposition of a precursor organometallic gas. These patterns served as markers which were used to optimize the focusing of the Ga ion beam without modifying the remainder of the surface. We then proceeded to sculpt the lens using a Ga beam voltage of 30 kV and current 48 pA. An electron beam was also used for imaging and monitoring the fabrication process. After finishing milling, we measured the actual profile of the lens using an atomic force microscope. The FIB milling rate was found to be about 0.24 $\mu m^3$ per nano Coulomb. We then modified the milling time to obtain the desired lens profile. A scanning electron microscope image of a lens of radius 1.5 μm made by FIB is shown in Fig. 45. In principle, this method should give greater control of the lens profile but we have not yet investigated the limits of this

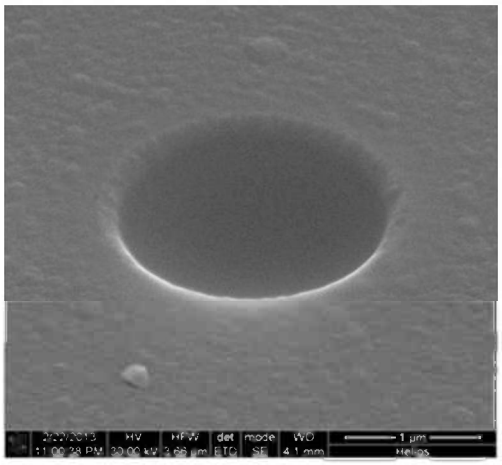


***Figure 45. Scanning electron microscope image of a $SiO_2$ lens of radius 1.5 μm***

in detail.

### *Performance Simulations of the Acoustic Microlenses*

To understand better the focusing action of the microlens we wrote a finite-difference time-domain FORTRAN program to simulate the sound propagation in the system. In order to concentrate on just the action of the lens, we did not consider the acoustics of the adjacent optical cavity, i.e., we took all of the material above the lens to be aluminum. In the initial condition the particle displacement and velocity were zero everywhere and there was a thermal stress in the layer of the aluminum lying between 1490 and 1740 nm above the planar interface between the aluminum and the water. The program used

isotropic linear elasticity for the aluminum and for sound propagation in the water included the effects of both shear and bulk viscosity. Absorbing boundary conditions were applied at all of the boundaries of the region in which the simulation was performed. To create these conditions we used the perfectly matched layer method introduced by Berenger.[36] As an example, we considered a lens with radius of curvature 2.5 μm and which subtended a semi-angle of 45 degrees. Results are shown in Fig. 46 for selected times; part a) shows the strain distribution before the sound has reached the top of the lens, b) is at a time just after the sound has crossed into the water, and c) and d) show the strain distribution just before and just after the sound reaches the acoustic focus. The figure shows the volume strain $\eta$ as a linear plot.

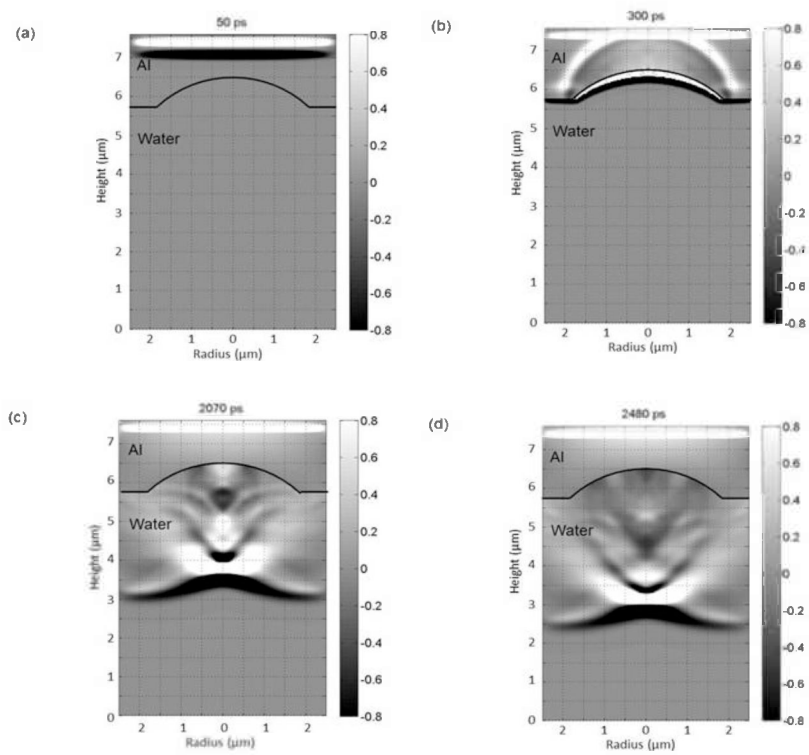


***Figure 46: Simulation of the sound propagation for a 2.5 μm radius lens with a 45° semi-angle. The volume strain is plotted on a linear scale, and is shown for times of 50 ps, 300 ps, 2070 ps and 2480 ps.***

### *Benchtop Experimental Proof-of-Concept Results*

In order to make measurements, the pump and probe beams have to be focused onto the area of the optical cavity directly above the lens. This is challenging because of the small size of the lens. To find the correct position we first direct the light beams to the general area of the lens; unless we are very fortunate this means that the beams are incident at a position above an unpatterned flat region of the thick aluminum film. At this first stage of the assessment we have not yet introduced the water between this film and the sample.

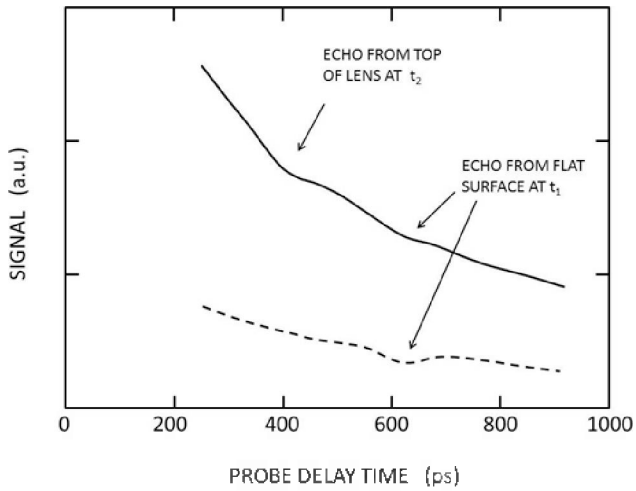


***Figure 47. Pump-probe data used to locate the acoustic lens. The dashed curve was obtained with the pump and probe beams at a position such that the sound is not incident on the acoustic lens. An echo is seen at time . The solid curve was obtained with the pump and probe beams directly above the lens resulting in an echo from the top of the lens. An additional echo is now seen at time .***

We then scan the time-delay of the probe beam relative to the pump spot and in this way detect the echo from the flat and free surface of the aluminum film. The result of the pump-probe measurement is shown as the dashed curve in Fig. 47. In this plot the data have been processed to remove the contribution from Brillouin oscillations arising from

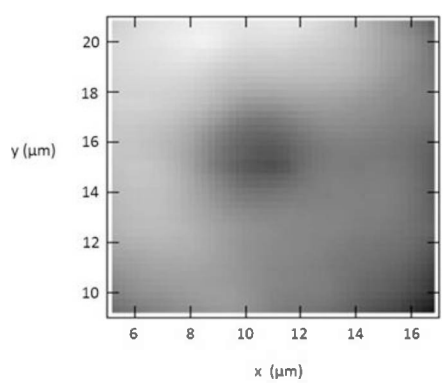


***Figure 48. Grey scale plot of the strength of the echo from the top of the lens as a function of position of the acoustic lens.***

sound propagating back in the glass substrate.[37] The echo arrives at around $t_1 = 620$ ps. The time-delay of the probe is then set fixed at this time and the lens structure is scanned in $x$ and $y$. This scanning was typically done in 0.5 μm steps and over a 15 μm range. When the pump and probe beams are directly above the lens, the echo from the flat and free surface is reduced in amplitude; it does not completely disappear because the area illuminated by the pump and probe beams extends somewhat beyond the area of the lens.

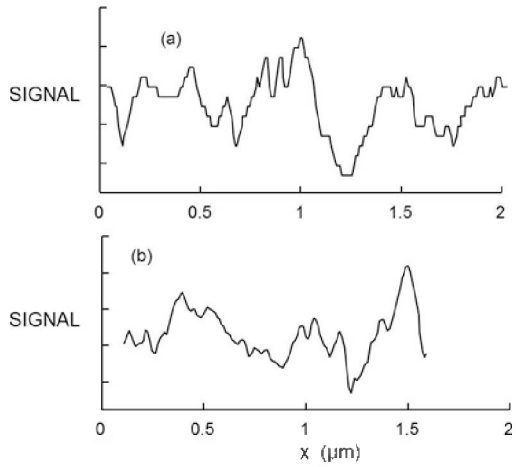


***Figure 49: Data obtained from a lateral scan over the samples described in the text. a) Data obtained on a trench sample with an aluminum lens, and b) data obtained with an SiO2 lens from the sample with profile shown in Fig. 50***

At the same position a new and earlier echo appears at time $t_2$ which comes from sound reflected from the top of the lens; this can be seen in the solid curve in Fig. 47. In Fig. 48 we show a grey scale plot of the signal strength at time $t_2$ as a function of position $xy$.

After locating the lens we then add the water coupling medium between the lens and the sample. The height of the sample is adjusted and the acoustic echo from the sample is detected. The sample is then translated laterally while the time delay of the probe light pulse is held constant and the height of the echo recorded. A scan is typically performed over a distance of 2 μm with a step size of 10 nm. In the experiment, signal to noise is a major problem and because of the required signal averaging even a scan over such a short distance and in one dimension takes 5 minutes.

For these first proof-of-concept experiments we have used the acoustic microscope to look at two samples (Fig.49). The first was a glass grating consisting of a series of trenches of width 270 nm, depth 220 nm, and repeat distance 550 nm, and measurements were made using an aluminum lens. A Fourier analysis of the signal as a function of $x$ gives a peak at a period of 540 nm in reasonable agreement with the sample period as measured by scanning electron microscopy.

The second sample was also based on bulk $SiO_2$ and had a period of 550 nm, with grooves of depth 450 nm. An SEM image is shown in Fig. 50. For this sample we used an $SiO_2$ acoustic lens made by the focused ion beam method. The lens had a radius of 2.5

µm. The data are shown in Fig. 49b and the period giving a best fit to the data was found to be 520 nm.

***Summary of SOAM results and outlook***

In this report we have outlined the concept, modeling by simulations, and initial experimental results for a proof-of-concept demonstration of a new type of high-frequency all-optical scanning acoustic microscope. In so doing we have built on our group's prior experience with picosecond ultrasonics while constructing a first version of a prototype instrument. A particularly critical new innovation has been the design and development of fabrication methods of an opto-acoustic micro-scale element which combines an acoustic focusing lens with an optical Fabry-Perot cavity. The performance of the lens was first simulated by numerical methods, to guide its experimental design in terms of the critical parameters. As for the lens fabrication, we have initially identified and implemented two rather different approaches, which give a useful basis for further

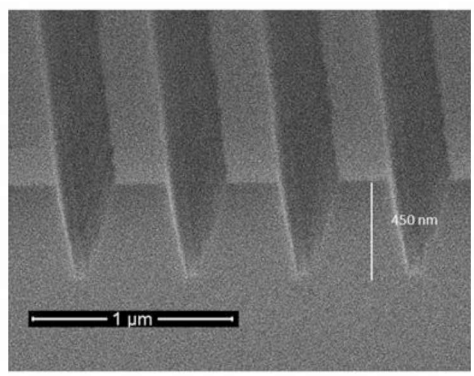


***Figure 50. SEM profile of the second $SiO_2$ sample. Data obtained on this sample are shown in Fig. 49b.***

development and improvement, e.g., of the control of the lens profile (curvature) and satisfying the nanoscale smoothness requirements. In terms of the overall scanning acoustic microscope instrument, work reported here has been limited to bench top demonstration of scanning surface profiles of grating-type surface corrugated SiO2 samples, with approximately 100 nm spatial resolution.

In the work performed so far we have certainly not reached the fundamental limits for the performance of this type of instrument. The present setup suffers from inadequate stability of the mechanical stage and poor signal to noise ratio. It should be

straightforward to improve stability of the stage. To improve the signal to noise, an improved detection system is required. The present optical cavity constructed using aluminum and silicon has a quality factor $Q$ of only 7. The $Q$ of the cavity could be greatly improved by using multiple dielectric films as the reflecting elements. If the pump and probe beams had different wavelengths, a separate absorbing film outside the cavity could be used to generate the sound.

The numerical simulations, suggest that a scanning instrument with resolution perhaps to 50 nm could be possible. An acoustic microscope of this type, properly engineered and manufactured as a high precision metrology tool, could be used for measurements of surface topography and also for measurements of the elastic properties of the material near to the surface of a sample, just as in a conventional acoustic microscope. Such a tool could have multiple applications for nondestructive metrology of complex structural features of semiconductor integrated circuits during large-scale wafer-level fabrication.

**II. Publications:**

"A Scanning Acoustic Microscope Based on Picosecond Ultrasonics", S. Che, P.R. Guduru, A.V. Nurmikko, and H.J. Maris, Ultrasonics (in press, 2014, available on line)

"Picosecond Ultrasonics Measurements Using an Optical Mask", Q. Miao, L.-W. Liu, T.J. Grimsley, A.V. Nurmikko, and H.J. Maris, Ultrasonics (in press, 2014, available on line)

T. J. Grimsley, F. Yang, S. Che, G. A. Antonelli, H. J. Maris and A. V. Nurmikko. "Ultrafast opto-acoustics applied to the study of material nanostructures." *Journal of Physics: Conference Series* **278**, 012037 (2011).

T. J. Grimsley, J. Ma, Q. Miao, A. V. Nurmikko, and H. J. Maris. "Picosecond Ultrasonic and Heat Flow Measurements with Enhanced Sensitivity," *Chinese Journal of Physics* **49** (1), 176 (2011).

T. J. Grimsley, F. Yang, G. A. Antonelli, H. J. Maris, and A. V. Nurmikko. "Experiments to Study the Propagation of Picosecond Sound Pulses in Water" *Chinese Journal of Physics* **49** (1), 151 (2011).

F. Yang, T. J. Grimsley, S. Che, G. A. Antonelli, H. J. Maris, and A. V. Nurmikko. "Picosecond ultrasonic experiments with water and its application to the measurement of nanostructures." *J. Appl. Phys.* **107**, 103537 (2010).

T.J. Grimsley, G. A. Antonelli, F. Yang, H.J. Maris, and A.V. Nurmikko. "Nanometer Metrology of Periodic Structures With Ultrafast Optoacoustics" in MRS Online Proceedings Library **1249**, 1249-F10-05 (2010).

"Picosecond Ultrasonic Measurements Using an Optical Cavity", Y. Li, Q. Miao, A.V. Nurmikko and H.J. Maris, Journal of Applied Physics **105**, 083516 (2009)

**III. Personnel working on the project**:

At Brown University, the project supported three doctoral graduate students: Tom Grimsley (graduated in 2013), Shan Che (graduated in 2014), and Li Wei Liu , all in the Physics Department and trained in experiment and advanced modeling and numerical simulation of ultrafast optoacoustics.

**V. Unexpended funds:** No unexpended funds are anticipated are left from the grant budget.

References:


1. Herzfeld, K. & Litovitz, T.A. *Absorption and dispersion of ultrasonic waves*. (Academic Press: New York, 1959).
2. Navier, C.L.M.H. Mémoires sur les lois du mouvement des fluides. *Mémoires de l'Académie des sciences de l'Institut de France* 389 (1823).
3. Sorokin, S.V. & Chubinskij, A.V. On the role of fluid viscosity in wave propagation in elastic plates under heavy fluid loading. *Journal of Sound and Vibration* 311, 1020-1038 (2008).
4. Long, Y. & Jiang, H. Rigorous Numerical Solution to Complex Transcendental Equations. *International Journal of Infrared and Millimeter Waves* 19, 785-790 (1998).
5. Kuhn, H.W. Finding roots of polynomials by pivoting. *Fixed points : algorithms and applications* 11-40 (1977).
6. Kuhn, H.W. & MacKinnon, J.G. Sandwich method for finding fixed points. *J Optim Theory Appl* 17, 189-204 (1975).
7. De Groot, P., Colonna de Lega, X., Liesener, J. & Darwin, M. "Metrology of optically-unresolved features using interferometric surface profiling and RCWA modeling." *Opt. Express* **16**, 3970-3975 (2008).8. De Groot, P., Darwin, M.J., Stoner, R., Gallatin, G.M. & De Lega, X.C. United States Patent: 7948636 - Interferometer and method for measuring characteristics of optically unresolved surface features. (2011).
8. Villarrubia, J.S. "Scanning electron microscope analog of scatterometry." *Proceedings of SPIE* 304-312 (2002).
9. Bingham, P.R., Price, J.R., Tobin, K.W. & Karnowski, T.P. "Semiconductor sidewall shape estimation." *J Electron. Imaging* **13**, 474 (2004).
10. Villarrubia, J.S., Vladár, A.E. & Postek, M.T. "Scanning electron microscope dimensional metrology using a model-based library." *Surface and Interface Analysis* **37**, 951-958 (2005).
11. Villarrubia, J.S. & Ding, Z.J. "Sensitivity of scanning electron microscope width measurements to model assumptions." *Journal of Micro/Nanolithography, MEMS and MOEMS* **8**, 033003 (2009).
12. Postek, M.T. & Vladár, A.E. "Modeling for accurate dimensional scanning electron microscope metrology: then and now." *Scanning* **33**, 111-125 (2011).
13. Lee, K.L. Submicron Si trench profiling with an electron-beam fabricated atomic force microscope tip. *J Vac. Sci. Technol. B* **9**, 3562 (1991).
14. Hafner, J.H., Cheung, C.L. & Lieber, C.M. "Growth of nanotubes for probe microscopy tips." *Nature* **398**, 761-762 (1999).
15. Nguyen, C.V. et al. "Carbon nanotube tip probes: stability and lateral resolution in scanning probe microscopy and application to surface science in semiconductors." *Nanotechnology* **12**, 363-367 (2001).
16. Nguyen, C.V. et al. "Carbon nanotube scanning probe for profiling of deep-ultraviolet and 193 nm photoresist patterns." *Appl. Phys. Lett.* **81**, 901 (2002).
17. Oon, C.H., Thong, J.T.L., Lei, Y. & Chim, W.K. "High-resolution atomic force microscope nanotip grown by self-field emission." *Appl. Phys. Lett.* **81**, 3037 (2002).
18. Strus, M.C., Raman, A., Han, C.-S. & Nguyen, C.V. "Imaging artefacts in atomic force microscopy with carbon nanotube tips." *Nanotechnology* **16**, 2482-2492 (2005).
19. Solares, S.D. & Chawla, G. "Exploration of AFM Imaging Artifacts Occurring at Sharp Surface Features When Using Short Carbon Nanotube Probes and Possible Mitigation With Real-Time Force Spectroscopy." *J. Manuf Sci. Eng.* **132**, 030904-14 (2010).
20. S.Y. Sokolov, U.S. Patent 2,164,265 "Means For Indicating Flaws in Materials," publication date June 27, 1939.
21. F. Dunn and W.J. Fry, **31**, 632 (1959).

22. R.A. Lemons and C.F. Quate, Appl. Phys. Lett, **24**, 163 (1974).
23. S.Y. Sokolov, U.S. Patent 2,164,265 "Means For Indicating Flaws in Materials," publication date June 27, 1939.
24. J. Rouch, C.C. Lai, and S.H. Chen, J. Chem,. Phys. **65**, 4016 (1976).
25. C. Thomsen, H.T. Grahn, H.J. Maris and J. Tauc, Phys. Rev. **B34**, 4129 (1986).
26. C.D. Zhu, H.J. Maris and J. Tauc, Phys. Rev. **B 44**, 4281 (1991).
27. F. Yang, T.J. Grimsley, S. Che, G.A. Antonelli, H.J. Maris and A.V. Nurmikko, J. Appl. Phys. **107**, 103537 (2010).
28. T.J. Grimsley, F. Yang, G.A. Antonelli, H. J. Maris, A. V. Nurmikko, Chinese Journal of Physics, **49**, 151 (2011).
29. Physik Instrumente, 16 Albert St, Auburn, MA 01501.
30. H. Ottevaere, R. Cox, H.P. Herzig, T. Miyashita, K. Naessens, M. Taghizadeh, R. Völkel, H.J. Woo, and H. Thienpont, J. Opt. A **8**, S407 (2006).
31. C.S. Lim, M.H. Hong, Y. Lin, , Q. Xie, B.S. Luk'yanchuk, A. Senthil Kuma, and M. Rahman, Appl. Phys. Lett. **89**, 191125 (2006).
32. C.S. Lim, M.H. Hong, A. Senthil Kuma, M. Rahman and X.D. Liu, Int. J. Machine Tools and Manufacture **46**, 552 (2006).
33. Triboindentor T900 from Hysitron, Inc., Minneapolis, MN 55344.
34. Helios 600 from FEI, Hillsboro, Oregon 97124.
35. J.P. Berenger, J. Comp. Phys., **114**, 185 (1994).
36. The origin and theory of Brillouin oscillations is discussed in H.N. Lin, R.J. Stoner, H.J. Maris and J. Tauc, J. Appl. Phys., **69**, 3816 (1991).